Microphysical Insights into Ice Pellet Formation Revealed by Fully Polarimetric Ka-band Doppler Radar

Matthew R. Kumjian* and Dana M. Tobin

Department of Meteorology and Atmospheric Science, The Pennsylvania State University, University Park, Pennsylvania, USA

Mariko Oue

School of Marine and Atmospheric Sciences, Stony Brook University, Stony Brook, NY

Pavlos Kollias

School of Marine and Atmospheric Sciences, Stony Brook University, Stony Brook, NY, and Brookhaven National Laboratory, Upton, NY

Corresponding author address: Department of Meteorology and Atmospheric Science, The Pennsylvania State University, 513 Walker Building, University Park, PA 16802

E-mail: kumjian@psu.edu

ABSTRACT

Fully polarimetric scanning and vertically pointing Doppler spectral data from the state-of-the-art, Stony Brook University Ka-band Scanning Polarimetric Radar (KASPR) are analyzed for a long-duration case of ice pellets over central Long Island from 12 February 2019. Throughout the period of ice pellets, a classic refreezing signature was present, consisting of a secondary enhancement of differential reflectivity Z_{DR} beneath the melting layer within a region of decreasing reflectivity factor at horizontal polarization Z_H and reduced co-polar correlation coefficient ρ_{hv}. The KASPR radar data allow for evaluation of previously proposed hypotheses to explain the refreezing signature. It is found that, upon entering a layer of locally generated columnar ice crystals and undergoing contact nucleation, smaller raindrops preferentially refreeze into ice pellets prior to the complete freezing of larger drops. Refreezing particles exhibit deformations in shape during freezing, leading to reduced ρ_{hv}, reduced co-to-cross-polar correlation coefficient ρ_{xh}, and enhanced linear depolarization ratio LDR, but these shape changes do not explain the Z_{DR} signature. The presence of columnar ice crystals, though apparently crucial for instigating the refreezing process, do not contribute enough backscattered power to affect the Z_{DR} signature, either.

1. Introduction

Freezing and frozen precipitation during winter storms can pose significant societal hazards. These storms can be disruptive to airline travel via aircraft icing (e.g., Bernstein et al. 1998), increase the risk of motor vehicle crashes on roadways (e.g., Black and Mote 2015; Tobin et al. 2020), and have the potential to cause power outages and property damage or loss (e.g., Rauber et al. 2001; Call 2010). The hazard of freezing precipitation lies primarily in the ice glaze produced on exposed surfaces that can weigh down and damage tree limbs and overhead wires, or slick sidewalks and roadways for pedestrian and vehicle traffic, whereas frozen precipitation (i.e., snow, ice pellets) can be less destructive with the absence of such ice glaze (e.g., Zerr 1997).

Two of these hazardous winter precipitation types – ice pellets and freezing rain – can form in similar environments in which warm (> 0 °C) air aloft overlies a near-surface cold (< 0 °C) layer. Snow may melt fully in the warm layer, and subsequently may (i) remain as supercooled liquid and freeze on contact with the surface (which we call freezing rain), or (ii) refreeze partially or fully into ice pellets prior to reaching the surface. Snow that partially melts may also refreeze (typically as irregular ice pellets) or reach the surface as slush. Details of the lower tropospheric thermodynamic profiles – perhaps subtle – may govern the fates of precipitation particles as they approach the ground. Such nuances create a forecasting and detection challenge (e.g., Ralph et al. 2005; Stewart et al. 2015). As such, additional means to detect or distinguish precipitation types are crucial.

Previous work has established that there is a dual-polarization radar signature associated with ice pellet formation in at least some cases (Kumjian et al. 2013; Kumjian and Schenkman 2014; Ryzhkov et al. 2016; Van Den Broeke et al. 2016; Tobin and Kumjian 2017; Nagumo et al. 2019). This hydrometeor "refreezing signature" is an enhancement of differential reflectivity (Z_{DR}) be-

neath the melting layer, typically collocated with the coldest point in the lower-tropospheric temperature profile, and usually is found within a layer of decreasing (towards the ground) radar reflectivity factor at horizontal polarization (Z_H). Subtle reductions in the co-polar correlation coefficient ($\rho_{\rm hv}$) are found in this layer, as well. The aforementioned studies collectively have found the refreezing signature, when present, is a robust indicator of ice pellets. Further, Tobin and Kumjian (2017) found that a descending refreezing signature can be used to forecast or anticipate a changeover in precipitation type from ice pellets to freezing rain.

The refreezing signature has been partly explained by Kumjian et al. (2013), hereafter K13. The reduction in Z_H towards the ground is well understood as the reversion of hydrometeor relative permittivity to that of ice from liquid at microwave frequencies (i.e., opposite of the contribution to enhanced Z_H in the melting layer "bright band"). However, although the large increase in fallspeeds upon melting is a major contributor to the appearance of the Z_H bright band bottom (e.g., Szyrmer and Zawadzki 1999; Zawadzki et al. 2005; Fabry 2015), such significant changes in hydrometeor fallspeeds typically are not present in the refreezing layer. The reduction in $\rho_{\rm hv}$ arises because of the diversity of particle shapes and likely increased wobbling of particles as they begin to freeze. Because the diversity in particle shapes is much less in the refreezing layer (where raindrops freeze into spherical or spheroidal ice pellets) compared to in the melting layer (where irregularly shaped snow aggregates acquire liquid water as they melt), the $\rho_{\rm hv}$ reduction is smaller in magnitude than in the melting layer. The $Z_{\rm DR}$ enhancement, however, has not been adequately explained, though several hypotheses have been put forward in the literature. These are described below, along with their limitations.

The first hypothesis to explain the $Z_{\rm DR}$ enhancement is preferential refreezing of smaller raindrops (K13). If the smaller raindrops freeze first, their contribution to the overall Z_H decreases, thereby increasing the relative contribution to Z_H from large raindrops. This results in an increase

in Z_{DR}, analogous to evaporation (Kumjian and Ryzhkov 2010; Xie et al. 2016) or size sorting (Kumjian and Ryzhkov 2012). Once all liquid drops freeze into ice pellets, the reduced relative permittivity and increased wobbling lead to a Z_{DR} reduction. Idealized calculations in K13 support this; however, microphysically it is inconsistent with expectations based on theory: via the immersion mode, larger drops should have a greater probability of nucleating and thus freezing, *ceterus paribus* (e.g., Bigg 1953; Vali 1994; Pruppacher and Klett 1997; Kumjian et al. 2012).

The second hypothesis is that pristine ice crystals, generated locally within the cold near-surface layer, contribute to increased Z_{DR} (K13). The presence of such pristine ice crystals could help kickstart freezing via contact nucleation. Small crystals falling into a subsaturated layer and sublimating and/or being captured during contact nucleation could explain their disappearance and thus reduction of Z_{DR} beneath the enhancement. However, the previous radar-based studies did not have evidence for such crystals, although 75% of the cases analyzed in Stewart and Crawford (1995) featured coincident observations of ice pellets and ice needles. Cortinas et al. (2004) found snow reported concurrently with ice pellets 37% of the time when ice pellets were reported in hourly surface observations across the United States and Canada.

Finally, Nagumo et al. (2019) recently argued that hydrometeor deformation or bulging during freezing leads to more extreme aspect ratios, and, prior to the onset of wobbling, this leads to increased Z_{DR} values. Once hydrometeors begin to wobble, Z_{DR} decreases. It is unclear from their study why wobbling would be delayed after the initial deformation of shape, because the change in a hydrometeor's cross-sectional area should directly affect its fall behavior. Further, the 2D-video disdrometer-observed aspect ratios reported in their paper are not very extreme, and no scattering calculations were performed to test whether such aspect ratio changes could explain the enhanced Z_{DR} signature.

The main goal of this study is to evaluate the previously published hypotheses on the emergence of the polarimetric refreezing Z_{DR} signature: (i) preferential refreezing of smaller drops (K13), (ii) the local generation of ice crystals in the near-surface cold layer (K13); (iii) particle deformation and wobbling behavior (e.g., Nagumo et al. 2019). We evaluate these hypotheses using novel observations from a prolonged ice pellet case over central Long Island, collected with Stony Brook University's fully polarimetric, Ka-band Scanning Polarimetric Radar (KASPR). These radar observations provide new microphysical insights into ice pellet formation and allow us to evaluate the hypotheses described above. The next section provides an overview of the ice pellet case and the radar dataset. Section 3 presents the data analysis, and section 4 is the discussion and conclusions.

2. Data and Case Overview

a. 12 February 2019 Event

At 12 UTC on 12 February 2019, a strong (1039-hPa) surface high over southeastern Canada helped to set up cold-air damming along the eastern slopes of the Appalachians. At the same time, a strong, negatively tilted upper-level trough was approaching from the Midwest. At 18 UTC, an associated strengthening surface low was present over Lake Michigan. This setup allowed for warm-air advection between roughly 700 and 900 hPa on the east side of the trough to override the near-surface cold, dry air present over the region, leading to a well-anticipated ice pellet event over Long Island.

Figure 1 shows the evolution of the vertical profiles of temperature and dewpoint temperature over Stony Brook, on Long Island. Unfortunately, no intermediate (18 UTC) sounding is available, so the 18 UTC profiles come from the RAP model analysis (Benjamin et al. 2016). The profiles' evolution reveals the formation and intensification of a warm air layer aloft owing to the low-level

warm-air advection. At 18 UTC, the warm air layer aloft was shallow, and the underlying cold air features a minimum of about -7 °C near 800 m AGL. Surface observations at nearby stations (not shown) suggest the 18 UTC RAP analysis has a negative temperature bias of 1-2 °. If this negative bias is also present aloft, the minimum temperature at 18 UTC may be closer to -5 °C, which is still supportive of ice pellets (e.g., K13) and does not affect the microphysical interpretation of our analysis.

The near-surface cold layer has moistened significantly in this time, in part owing to precipitation falling into the layer. By 00 UTC, the warm nose has increased in magnitude and depth, with the surface temperature exceeding 0 °C. The evolution of these profiles would suggest a transition from snow to ice pellets/freezing rain, and ultimately to rain over the 12-hour period.

Indeed, precipitation type observations from around the region confirm the transition from snow to ice pellets and/or freezing rain, and finally rain at most sites (Fig. 2). All human-augmented observing stations (LGA, ISP, JFK, HPN) reported ice pellets (PL) for a several-hour period beginning around 16 UTC. Non-augmented observing stations are only capable of reporting RA and SN, so "unknown precipitation" may be PL (e.g., Jones et al. 2004; Tobin and Kumjian 2017). Observations at ISP (the closest reporting station to Stony Brook University) reported PL from 1622 UTC to 2308 UTC, with concurrent observations of freezing rain (FZRA) from 1651-1729 UTC, and snow (SN) from 1405-1654, 1800-1912, and 1952-2023 UTC. Rain (RA) began there at 2153 UTC.

Data from the nearby WSR-88D radar KOKX may be summarized in time-height form using quasi-vertical profiles[1] (QVPs; K13, Ryzhkov et al. 2016; Kumjian and Lombardo 2017). In particular, we apply a variant referred to as range- and azimuth-defined QVPs (raQVPs; Tobin

[1]Quasi-vertical profiles are constructed by averaging PPI data azimuthally at each range gate, and converting each range gate to height above the radar. This facilitates displaying vertical profiles of the dual-polarization radar variables.

and Kumjian 2017) that are shown in Fig. 3. The data come from the ranges and azimuths over SBU, as indicated by the purple wedge in Fig. 2, where range has been converted to height above the KASPR. Thus, all radar data and analyses are shown with the same vertical coordinates of height above the KASPR (or above radar level, hereafter "ARL"), which is located $\sim$2 m AGL and 48 m above sea level. The emergence of the melting layer just after 1600 UTC is consistent with surface reports of ice pellets and freezing rain around this time (cf. Fig. 2). A refreezing signature in Z_{DR} (Fig. 3b) becomes prominent at about 1730 UTC, around the cessation time of freezing rain at ISP. The Z_{DR} enhancement associated with refreezing starts at about 1 km ARL, but quickly descends to $\sim$700 m ARL by 1800 UTC. Throughout the next few hours, the melting layer height increases, implying a deepening of the warm nose associated with warm-air advection. The refreezing signature persists until at least 2200 UTC, after which precipitation becomes sparser as indicated by reduced Z_H, and ISP begins reporting rain.

b. Stony Brook University KASPR

The Stony Brook University (SBU) KASPR is a state-of-the-art system operated from the SBU campus. Technical specifications of KASPR are provided in Table 1. Its 0.32° beamwidth and 2.2-kW peak power offer fine resolution and good sensitivity well-suited for winter precipitation studies. Of particular interest for this study is its *fully polarimetric* capabilities; that is, by switching transmit polarizations from pulse to pulse while receiving simultaneous horizontal (H) and vertical (V) polarizations, it measures all components of the covariance matrix described in, for example, Ryzhkov (2001).

In addition to the typical suite of polarimetric radar measurements, including reflectivity factor at horizontal polarization Z_H, differential reflectivity Z_{DR}, differential phase shift Φ_{DP}, and the co-polar correlation coefficient ρ_{hv}, KASPR's fully polarimetric capabilities allows for measure-

ments of the linear depolarization ratio LDR, the co-to-cross-polar correlation coefficients ρ_{xh} and ρ_{xv}, and the cross-polar differential phase shifts Φ_{xh} and Φ_{xv}. Only a few studies have explored these quantities theoretically (e.g., Ryzhkov 2001; Moisseev et al. 2002) or observationally (e.g., Ryzhkov et al. 2002; Melnikov et al. 2019). Whereas ρ_{hv} decreases for larger pulse-to-pulse variations in Z_{DR} (i.e., greater diversity of Z_{DR} for scatterers within the radar sampling volume), ρ_{xh} decreases for larger pulse-to-pulse variations in LDR (i.e., greater diversity of LDR within the sampling volume). Thus, increases in canting angle dispersion or emergence of irregular shapes can reduce ρ_{xh}. However, cross-coupling of the co- and cross-polar channels positively bias ρ_{xh} in regions of low intrinsic ρ_{xh}, such as may be expected in pure rain (e.g., Moisseev et al. 2002; Melnikov 2006). A conceptual description of these quantities is included in the Appendix.

During the ice pellet event, KASPR executed a scanning strategy that consisted of a surveillance (PPI) scan at 15° elevation angle, hemispheric range-height indicator (HRHI) scans at four azimuth angles (0°, 45°, 99°, which is towards KOKX, and 135°), and a 5-minute vertically pointing mode (VPT) during which Doppler spectrum data were collected. This pattern was repeated and took approximately 15 minutes to complete. The PPI and HRHI scans were performed with a full polarimetry mode and scan speeds of 6° s^{-1} and 2° s^{-1}, respectively, to collect data with a 30-m range-gate spacing, 0.6° PPI azimuthal spacing and 0.3° HRHI elevation spacing. The VPT mode was executed with only horizontally polarized waves transmitted and both horizontally and vertically polarized waves received. Thus, Z_{DR} and Φ_{DP} are unavailable for VPT scans, but LDR and ρ_{xh} are. During the VPT mode, the Doppler spectra were collected every second with a 15-m range-gate spacing and 0.04 m s^{-1} velocity bin spacing.

3. Observational Analysis

QVPs obtained from the KASPR 15° elevation angle PPI scans are plotted in Fig. 4 for the event in height versus time. The color bars and scaling are identical to Fig. 3 for direct comparison of the KASPR QVPs to the KOKX range- and azimuth-defined QVPs. The physical sampling space of each plot varies as a result of the methodological differences between the two averaging techniques; however, both are sufficient to identify locations of the melting and refreezing layers contained with approximately 2-3 km and 0.5-1 km, respectively. Note there is no "bright band" signature at Ka band owing to the impact of resonance scattering effects of large, wet snow aggregates (e.g., Kollias and Albrecht 2005). The refreezing signature is clearly evident in the KASPR QVPs as enhanced $Z_{\rm DR}$, reduced $\rho_{\rm hv}$, and enhanced LDR. It is evident that the KASPR has improved resolution of these features over KOKX.

Figure 5 shows PPIs of polarimetric fields at 1817 UTC when PL were ongoing at the radar location. Z_H (Fig. 5a) shows a clear transition from ice to liquid, with larger Z_H values caused by the greater relative permittivity of liquid, and again without a "bright band" for the reason mentioned above. Within about 3 km range of the radar, a noticeable decrease in Z_H occurs as the hydrometeors freeze and the relative permittivity reverts back to that of ice. $Z_{\rm DR}$ (Fig. 5b) shows a remarkable double-ring enhancement structure, with the outer ring indicating the melting layer, and the inner ring indicating the refreezing layer; this is the classic refreezing signature (K13). LDR (Fig. 5c) shows an enhancement in the melting layer as nonspherical ice particles acquire liquid water via melting (increased relative permittivity) and wobble. The sudden reduction of LDR occurs when these particles collapse into spheroidal raindrops with more stable orientation and symmetric shapes. Near the surface (within 5 km radius), a subtle LDR enhancement of ~ 3 dB is evident, indicating some degree of scattering asymmetry, either through enhanced wobbling

or the emergence of irregular shapes. Figure 5d shows the $\Phi_{\rm DP}$ field, which exhibits a double-ring enhancement structure similar to that of $Z_{\rm DR}$. In both cases, the local enhancements are associated with co-polar backscatter differential phase ($\delta_{\rm co}$), originating from nonspherical, wet hydrometeors large enough relative to the wavelength to cause resonance scattering. The difference is that the melting layer features large, melting aggregates, whereas the refreezing layer contains partially frozen/refreezing raindrops. The co-polar correlation coefficient (Fig. 5e) shows a clear reduction in the melting layer, followed by increased values near 1.0 in the pure-liquid layer. In the layer of refreezing near the surface, there is a subtle decrease in $\rho_{\rm hv}$ to about 0.98, indicative of more diversity of hydrometeor shapes as they either begin wobbling or acquire irregularities. Gibson and Stewart (2007) found that 9% of ice pellets observed at the ground during winter storm were aggregates of 2-5 individual ice pellets. Though such aggregates would contribute to reduced $\rho_{\rm hv}$ and increased LDR, the monotonically decreasing Z_H, increase of $\rho_{\rm hv}$, and decrease of LDR below this layer argue against such aggregates contributing significantly to the observed signatures. Finally, the $\rho_{\rm xh}$ field (Fig. 5f) shows two reductions: one in the melting layer, and one in the refreezing layer (mirroring LDR), where the reductions indicate a diversity of LDR values owing to irregular, wet particles with some distribution of wobbling. The minimum value of $\sim$0.3 in the pure-rain region is a bias owing to some combination of cross-coupling by the antenna (e.g., Ryzhkov et al. 2002; Moisseev et al. 2002) and low SNR (Melnikov 2006).

The PPI data are summarized as QVPs in Fig. 6. These reveal a steady increase towards the ground in Z_H and $Z_{\rm DR}$ in the pure rain layer[2]; this may be a manifestation of raindrop coalescence (Kumjian and Prat 2014) or attenuation and differential attenuation through the layer. For $\sim$30

[2]It is assumed that particles beneath the melting layer but above the refreezing layer are pure liquid drops, given that the radar data clearly show spherical/spheroidal hydrometeors and there are no indications of freezing until these hydrometeors have fallen well into the < 0 °C layer. However, we cannot rule out the possibility that the larger hydrometeors still contained small amounts of melting ice in their cores.

dBz in rain, Matrosov (2005) suggests one-way specific attenuation is < 1 dB km^{-1}. This, and the fact that $\Phi_{\rm DP}$ changes through this layer are minimal, suggest that attenuation and differential attenuation are not the major contributors. The increase in $Z_{\rm DR}$ within the refreezing layer begins around 900 m ARL (i.e., 3.6 km range at 15° elevation angle), whereas the decrease in Z_H occurs slightly below this point. The peak in $Z_{\rm DR}$ occurs between 500 and 600 m ARL, squarely in the middle of the reduction of Z_H. The LDR peak is just below 400 m ARL (though LDR starts increasing at about 700 to 800 m), which is below the $Z_{\rm DR}$ peak. The $\Phi_{\rm DP}$ trace is similar to that of $Z_{\rm DR}$, suggesting the same underlying physical processes. At Ka band, small-to-medium-sized (1-4-mm equivalent volume spherical diameter) raindrops that produce enhanced $Z_{\rm DR}$ can also produce significant backscatter differential phase $\delta_{\rm co}$ (e.g., Matrosov et al. 1999, their Fig. 3). Given that the observed $\delta_{\rm co}$ is an integration of signals from particles in the sampling volume, it would respond similarly to $Z_{\rm DR}$, which may explain the strong similarities of the observed profiles. The $\rho_{\rm hv}$ minimum is found just above 400 m ARL, between the $Z_{\rm DR}$ and LDR peaks, whereas the $\rho_{\rm xh}$ reduction occurs coincident with the increase in LDR.

Hemispheric RHIs with KASPR provide additional microphysical insights (e.g., Kollias et al. 2014). Figure 7 shows a portion of the HRHI scan from 1813 UTC, when a well-developed refreezing signature was present. A decrease in Z_H around 0.5 km ARL is evident, as before, associated with the change in relative permittivity as particles refreeze. The dual $Z_{\rm DR}$ enhancements associated with melting (at just below 2.5 km ARL) and refreezing (just above 0.5 km ARL) are evident at lower antenna elevation angles, but diminish as the antenna elevation moves towards zenith pointing. This indicates that hydrometeors are either (a) isometric when viewed from below, as is true for spherical or oblate particles with their maximum dimension in the horizontal plane, on average, or (b) irregularly shaped particles have no preferred orientation in the horizontal plane, such that on average $Z_{\rm DR}$ is 0 dB (analogous to random orientations leading to 0 dB for

side incidence). The HRHIs of ρ_{hv} (Fig. 7c) and LDR (Fig. 7d) provide the answer. For both HRHIs, the melting and refreezing layers are clearly visible as reduced ρ_{hv} or enhanced LDR, even when the antenna is pointing at zenith. This implies a diversity of shapes for particles when viewed from below, including some whose major axes do not align with the principal polarization directions. In other words, the particles in both the melting and refreezing layers do not have rotational symmetry about a vertical axis, but rather are irregular with their maximum dimensions in the horizontal plane having no preferred azimuthal orientation. However, the refreezing layer signals are far weaker than those in the melting layer, indicating far less particle anisotropy.

As an assessment of the refreezing signature's robustness, we extracted vertical profiles from ranges -3 to -4 km in the HRHI, and binned the data into 100-m increments. Data in each 100-m bin were averaged, and the standard deviation of data within the bin was computed. Despite more subtle magnitudes to these refreezing layer signatures, averaged vertical profiles (and the variability about the mean) extracted from the RHI (Fig. 8) demonstrate that these features are statistically significant insomuch as the changes in the mean are greater than the variability about that mean, indicated by ± 1 standard deviation error bars.

As part of the scanning sequence, the KASPR antenna was pointed vertically and rotated for a 5-minute period, during which spectral data were collected. An example of a time-height plot of the average moments during such a zenith-pointing scan are shown in Fig. 9. Figure 9a reveals fallstreaks in snow and rain, and the reduction in Z_e near the surface associated with refreezing. The mean Doppler velocity (Fig. 9b) also shows the clear transition from snow to rain at the melting layer as the rapid increase in fallspeeds. Note our convention is negative radial velocities indicate scatterers moving towards the radar (i.e., falling). Within the refreezing layer, however, we do not see large reduction of fallspeeds as is reported in some studies (e.g., Nagumo and Fujiyoshi 2015; Bukovčić et al. 2017), but rather increased variability in mean Doppler velocity presumably

owing to boundary-layer turbulence beneath the inversion. This is also evident from the HRHI in Fig. 7e, and in the Doppler spectrum width field (not shown). LDR shows a clear increase in the refreezing layer, coincident with a decrease in ρ_{xh}. The decrease in ρ_{xh} and increase in LDR from this vertically pointing mode indicate asymmetries in the horizontal plane (when viewed from below) during refreezing. The time-averaged profiles (Fig. 10) show these features clearly. The ± 1 standard-deviation error bars indicate the robustness of the signals.

The Doppler spectra collected during the vertically pointing scan offer additional microphysical insights. We tested several methods of censoring the noise from the spectra presented here. For example, we estimated the mean noise level at each height from the co-polar spectral power, the standard deviation about that mean, and censored any data within 5 standard deviations of the noise estimate (e.g., Li and Moisseev 2020). We also examined more stringent thresholds, including multiple values of co-polar spectral power well above the estimated noise floor. Doing so revealed that the less stringent thresholds resulted in positively biased LDR at the edges of the spectra, despite having signals well above the noise floor. As such, we went with a stringent -70-dB threshold in co-polar power (this is approximately 20 dB above the estimated noise floor). This threshold is applied to all spectral data presented herein. Instantaneous spectra at 1822:57 UTC are shown in Fig. 11. We also take a 30-s average[3] of the spectra to bring out the robust features and reduce the statistical fluctuations owing to noise. Figure 12a shows the spectral reflectivity (equivalent reflectivity factor Z_e as a function of radial velocity v_r and height), whereas Fig. 12b is the standard deviation of this average to highlight regions where the data are more variable.

[3] Averages are taken by velocity bin assuming the spectra are static. Some layers feature turbulence and shifts in the spectra, which are evident in the standard deviation about the averages. Most of the spectra do not display significant changes in the peak location over the 30-s averaging period (see the Supplemental Material for animations).

Similar depictions of spectral LDR and spectral $\rho_{\rm xh}$ are shown in Figs. 13 and 14, respectively. Animations of these spectra are available as part of the online Supplemental Material.

Beneath the melting layer (but above the refreezing layer), several features of note appear in the instantaneous spectral Z_e (Fig. 11a) as well as the averaged spectral Z_e (Fig. 12). A few new-particle modes appear, including one at about 1300 m ARL associated with $v_r = -1$ to -2 m s^{-1}, and one at about 750 m ARL and -0.5 m s^{-1}. The upper new-particle mode emerges just beneath a shear layer evident in the HRHI of mean Doppler velocity (Fig. 7e) at the base of the warm air aloft, and could be new particle formation associated with turbulence[4] in this layer. Figures 11b and 13a reveal low LDR values for this mode, strongly suggesting liquid drops and thus drizzle formation. In contrast, the lower secondary spectral peak originates in the near-surface cold layer and exhibits enhanced LDR values (Figs. 11, 13a) and reduced $\rho_{\rm xh}$ values (Figs. 11c, 14a) suggestive of ice crystals and will be discussed in detail below.

In addition to the new spectral peaks, there is a noticeable reduction in the spectral Z_e starting around 600-700 m ARL (a result of refreezing and reversion of the relative permittivity back to that of ice), with a slope such that the drop-off in Z_e appears to occur at lower altitudes for faster-falling hydrometeors (particularly evident in the averaged Fig. 12a). There is also a general LDR enhancement for the entire spectrum in this layer, with larger values for the larger (faster-falling) hydrometeors (Fig. 13a). Similarly, the faster-falling hydrometeors exhibit somewhat lower $\rho_{\rm xh}$ values in this layer than their slower-falling counterparts (Fig. 14a), which suggests more nonsphericity, wobbling, and/or shape irregularities upon freezing.

---

[4]The animations of these spectragraphs suggest turbulence here, as does the slight lateral extension of the standard deviation of spectral Z_e shown in Fig. 12b. Turbulent positive vertical velocity perturbations would lead to increased saturation ratios, which, if sufficiently large, could activate new droplets. Turbulence may also augment collision-coalescence of droplets to promote drizzle formation (e.g., Shaw et al. 1999). See also Houze and Medina (2005).

To further elucidate the microphysical processes ongoing in this refreezing signature, we averaged the spectral Z_e and LDR within velocity bins in 0.5-m s^{-1} increments for velocity bins characteristic of raindrops (fallspeeds > 3 m s^{-1}; Figs. 15a,b). This range of velocity bins is also consistent with the reduction in Z_e seen in Fig. 12a. Because of the size-dependence of Z_e, we normalized the spectral Z_e values to display the patterns more clearly on the same scale. These normalized spectral Z_e profiles reveal that all fallspeed bins exhibit substantial decreases in Z_e towards the ground associated with refreezing, with the smaller size bins experiencing their Z_e decrease at higher altitudes (Fig. 15a). Similarly, all fallspeed bins exhibit LDR increases towards the ground, with larger fallspeed bins revealing greater LDR magnitudes (Fig. 15b).

We also compute the vertical gradients (defined towards the ground, so that positive values indicate increases towards the ground, and negative values indicate decreases towards the ground) of Z_e and LDR, which are plotted as a function of size bin in Figs. 15c,d. These data clearly show maximum negative Z_e gradient magnitudes at higher altitudes for the slower-falling hydrometeors. In other words, the smaller drops are undergoing their relative permittivity change as a result of refreezing further aloft than the larger drops. (In fact, given the negative Z_e gradients and positive LDR gradients present for the largest 3 velocity bins, these largest drops likely have not yet fully frozen at the bottom of the layer shown in Fig. 15.) The increase in LDR towards the ground (positive gradient values) follow a similar trend with particle size, though less clearly than the Z_e gradients. Note that these changes are within a 200-300-m layer, so they occur rapidly. The negative $\frac{\partial Z_e}{\partial z}$ occur exactly where the enhanced $Z_{\rm DR}$ peak is found within the refreezing layer (cf. Figs. 6, 8). This and the fact that small drops are refreezing at higher altitudes provides strong observational evidence for the "preferential refreezing" hypothesis of K13 outlined above. However, it does not explain *why* the small drops are preferentially refreezing first. To do that, we turn focus our attention on the cold-layer secondary spectral peak.

Spectra for 3 range bins (heights above the radar) from the vertical scan starting at 1820 UTC containing this new hydrometeor mode identified at ∼700 m ARL and $v_r > -0.5$ m s^{-1} (hereafter "secondary peak") are shown in Fig. 16. The secondary peak is clearly > 10 dB above the surroundings (and ∼20 dB above the noise floor, not shown), indicating it is not a spurious artifact or noise. Further, the animations of these spectra (see the Supplemental Material) show the peak wobbling about and responding to turbulence similarly to the rest of the spectra. This provides strong support that the secondary peak is a physical signal of a secondary mode of precipitation forming at altitudes below 1 km. When consulting the spectral LDR (Fig. 16, bottom panel), we see enhanced values for this spectral feature (up to about -15 dB), well above those of the main peak, consistent with the averaged spectra shown earlier. Such values are suggestive of highly nonspherical particles like columnar ice crystals. According to the RAP-analyzed temperature profile, the temperature at the level at which this secondary spectral peak emerges is approximately -7 °C (cf. Fig. 1). Ice crystals growing by vapor deposition between -3 and -8 °C have columnar habits (e.g., Bailey and Hallett 2009). Columnar ice crystals with fallspeeds of a few tenths of a m s^{-1} have maximum dimensions < 1 mm (e.g., Kajikawa 1972). The observed LDR values are consistent with such columnar crystals, according to scattering calculations and observations reported in Oue et al. (2015), as well as the range of LDR values (-14 to -18 dB) reported for columnar crystals at vertical incidence several other studies (e.g., Matrosov 1991; Aydin and Walsh 1999; Matrosov et al. 2001; Reinking et al. 2002). Thus, the available data strongly suggest the local generation of columnar ice crystals in the near-surface cold layer.

Do these columnar ice crystals contribute to the observed polarimetric refreezing signature, as alternatively hypothesized in K13? Following Oue et al. (2015, 2018), we can estimate the contributions of the main precipitation spectral peak (associated with the rain/ice pellets) and from this secondary peak to the overall Z_e and LDR by integrating over the power contained in subsets

of the velocity bins. To do this, we define the secondary peak as the power contained between 0 and -0.61 m s^{-1}, and the main peak from -0.85 m s^{-1} to -9 m s^{-1} (these thresholds were varied by several bins in either direction and the results are not significantly different). Over the 5-minute vertically pointing scan at 1820 UTC, the integrated main peak Z_e is consistently between about 30 and 35 dBz, whereas the integrated secondary peak Z_e is below -10 dBz (Fig. 17). In contrast, the main peak LDR is at the system lower limit (approximately -30 dB), whereas the secondary peak has LDR between about -15 and -21 dB. The secondary peak's contribution to the overall Z_e is thus more than 40 dB lower than the Z_e contribution from the main precipitation peak. Thus, even if the columnar crystals had extremely large intrinsic $Z_{\rm DR}$, their overall contribution to Z_e is so small that the total observed $Z_{\rm DR}$ would be unaffected. So, although crystals are generated locally (as hypothesized by K13), they do not contribute to the observed refreezing signature in this case.

But, do these columnar crystals have any relationship to the refreezing process? Do the crystals originate from splintering during drop freezing (e.g., Koenig 1965; Pitter and Pruppacher 1973; Chisnell and Latham 1976; Lawson et al. 2015), or are the crystals generated by other means but then facilitate raindrop freezing through contact nucleation? Or, are they not involved at all? For example, some studies (e.g., Hobbs 1965; Alkezweeny 1969; Czys 1989) have proposed that collisions between supercooled liquid drops may initiate freezing, which may be related to a deformation or distortion of the drop's liquid-air interface upon colliding with another (Fukuta 1975; Yang et al. 2018, 2019).

To help provide insight into this "chicken-or-the-egg" type question, we construct time-height depictions of the main and secondary (ice crystal) peak Z_e and LDR (Fig. 18). The secondary peak's -19-dBz Z_e contour (a conservative estimate of its emergence level from Fig. 18b) is overlaid on all panels for reference. In Fig. 18a, the main peak Z_e features a significant decrease

towards the ground centered at about 500 m AGL. The secondary peak's −19-dBz contour is located well above the sharpest gradient in main peak's Z_e. This implies that the columnar ice crystals appear several hundred meters above the greatest change in relative permittivity of the larger hydrometeors undergoing refreezing. When consulting the main peak's LDR (Fig. 18c), we see clearly that appreciable increases in LDR occur well below this −19-dBz contour, as well[5]. This means that deformations or irregularities in the refreezing hydrometeors occur well below where the columnar crystals appear. On the other hand, the main peak's enhanced LDR field follows very closely the −19-dBz contour, suggesting that the same physical mechanisms are involved.

So, to address the "chicken-or-the-egg" question: if the columnar crystals were a result of the refreezing raindrops splintering, *such splintering would have to occur prior to significant amounts of liquid freezing (responsible for the relative permittivity decrease) and prior to the appearance of any significant deformities or irregularities in the freezing drop shapes*. On the other hand, the hypothesis of locally generated ice crystals jump-starting the freezing process through contact nucleation is supported by these observations. Contact nucleation would initiate the freezing process, which would progress for some time (∼10s of seconds for the larger drops; e.g., Kumjian et al. 2012) before the raindrops completely freeze, creating some vertical separation between the level of nucleation and the subsequent observable response in the radar variables. The presence of columnar ice crystals prior to raindrop refreezing also would help explain the preferential refreezing of smaller drops first – as these are unlikely to nucleate first owing to immersion freezing (e.g., Pruppacher and Klett 1997). Rather, contact nucleation could instigate the process at more-or-less

[5]The drop-off in the secondary peak's Z_e at about 260 s occurs when the peak drops below the stringent −80-dB spectral power lower limit set for these plots, and thus is censored. However, it still appears as a local peak in spectral power above its adjacent velocity bins at these times (not shown).

the same time for all raindrops falling into the layer, but the longer timescale for freezing larger drops (e.g., Pruppacher and Klett 1997; Kumjian et al. 2012) means they would completely freeze at lower altitudes than smaller drops. Thus, the smaller drops finish freezing prior to the larger drops, leading to the observed Z_{DR} enhancement associated with the classic refreezing signature.

What is the origin of these small columnar ice crystals? The Stony Brook University radar observatory also has a Vaisala ceilometer and a Doppler lidar. Observations from these during the event (Fig. 19) reveal signals of several liquid layers, including the primary cloud base ($\sim$400 – 500 m AGL), as well as another in the $\sim$900 – 1000 m AGL layer. This latter signal indicates supercooled liquid droplets just above the layer where KASPR observes the secondary spectral peak associated with the columnar ice crystals. We speculate that the presence of these liquid cloud droplets may have facilitated ice nucleation, though the exact mechanism is unknown (particularly given the relatively high temperature; see, e.g., Kanji et al. 2017, and references therein).

4. Summary and Discussion

A long-duration ice pellet event occurred over Long Island on 12 February 2019 and was well-sampled by the Stony Brook University Ka-band Scanning Polarimetric Radar (KASPR). The KASPR observations revealed a classic hydrometeor refreezing signature first described by Kumjian et al. (2013), but the versatile scanning, Doppler spectral, and fully polarimetric capabilities of KASPR provided novel insights into the origins and microphysical processes leading to the hydrometeor refreezing signature. This new information allows us to evaluate published hypotheses on the refreezing signature's origin, namely preferential refreezing of smaller drops (Kumjian et al. 2013), local generation of ice crystals in the near-surface cold layer (Kumjian et al. 2013), and particle shape deformations/bulging and changes to the orientation distributions during freezing (Nagumo et al. 2019).

PPI scans of the refreezing signature at Ka band show similarities to previous signatures documented at S and C bands; namely, an enhanced Z_{DR} coincident with a reduction in Z_H within the near-surface cold layer, as well as reduced ρ_{hv}. For the first time, with KASPR we also find the refreezing layer (at least in this case) characterized by low ρ_{xh}, enhanced LDR, and enhanced δ_{co}. The close correspondence of Z_{DR} and δ_{co} features strongly suggests the same underlying physics is responsible for both. Preferential refreezing of smaller raindrops first would reduce their contribution to the total Z_H and thus increase the relative contribution of larger drops with larger intrinsic Z_{DR} and δ_{co} at Ka band. Owing to their small size and low relative permittivity, ice crystals would not produce appreciable δ_{co} at Ka band. Similarly, deformed ice pellets could be resonance scatterers at Ka band, but owing to the low imaginary part of the relative permittivity of ice at this wavelength, δ_{co} is negligibly small.

Hemispheric RHIs reveal the enhanced LDR and reduced ρ_{hv} and ρ_{xh} signals at vertical incidence in the refreezing layer, suggesting the hydrometeor asymmetries introduced during freezing are not favored in any particular plane. Randomly oriented deformities in the particle shape owing to freezing/bulging could explain the signatures. However, LDR "recovers" to some extent in the QVPs beneath the refreezing layer, after total freezing. This strongly suggests that the presence of liquid in partially frozen particles is the leading contributor to amplifying the asymmetries, whether viewed at side incidence (PPIs) or vertical incidence (vertically pointing scans and/or hemispheric RHI scans). Freezing by contact nucleation would initiate ice at some point or points on the particle surface, which would subsequently spread around the outside and then inward (e.g., Pruppacher and Klett 1997). This would lead to asymmetric liquid regions in the otherwise spherical/spheroidal particle, which would more substantially enhance LDR than deformities (e.g., bulges, spikes or other irregular shapes) in a completely frozen ice particle owing to the difference in relative permittivity between liquid and ice. Such deformities in a partially frozen

particle could also lead to asymmetric shapes of the liquid portion, which could also enhance the LDR.

The Doppler spectra from KASPR's vertically pointing scans confirm that the small drops undergo freezing first, providing strong evidence for the "preferential refreezing of smaller drops" hypothesis. As shown by idealized calculations in Kumjian et al. (2013), such preferential refreezing of small drops will lead to a Z_{DR} enhancement similar to that observed. The KASPR spectral data also show that the largest negative Z_e gradients (implying decreases towards the ground) and positive LDR gradients (implying increases towards the ground) occur at progressively lower heights for faster-falling and presumably larger particles. The spectra also reveal the presence of small columnar ice crystals emerging just above the refreezing layer; however, their overall contribution to Z_H (and thus Z_{DR}) is negligible. The crystals appear above the level where significant changes to larger hydrometeors' relative permittivities or shapes, strongly suggesting they do not result from splintering during freezing. Rather, if generated locally by some other means, they could facilitate rapid refreezing through contact nucleation. The origin of these columnar crystals, however, remains a mystery. Additional cases should be analyzed to understand the prevalence of these small ice crystals and to determine their importance for ice pellet formation in general.

In summary, KASPR observations provided substantial microphysical insights into ice pellet formation for the 12 February 2019 event. The data provide strong support for the hypothesis that preferential refreezing of smaller drops leads to the observed dual-polarization refreezing signature (particularly in Z_{DR}). In this case, small ice crystals generated locally appear to have contributed to nucleation of all drops falling into the layer via contact nucleation. The smaller fallspeeds and shorter times to complete freezing for the smallest drops allowed them to completely freeze at altitudes above the total freezing of larger drops, leading to the observed refreezing signature. The crystals did not provide sufficient Z_H to affect the observed Z_{DR} enhancement. Further, there

is no need to implicate complicated orientation behaviors of bulged particles to explain the Z_{DR} signature (Nagumo et al. 2019), though asymmetries arising during the freezing process (whether bulges or asymmetric liquid regions within a freezing particle) *are* likely given the signals in LDR, ρ_{hv}, and ρ_{xh}. The Z_{DR} enhancement from preferential refreezing of small drops may be augmented if the liquid portion within refreezing particles deforms considerably (i.e., to axis ratios more extreme than the particle itself and/or those of equivalent-sized raindrops) as a result of bulging or asymmetric freezing, and the particle orientation does not change appreciably during this process. The analysis presented here is from a single case, so clearly more well-documented events are needed to determine the generality of the findings from this study. The advent of advanced, fully polarimetric Doppler observations such as those available from KASPR will improve our understanding of microphysical processes, especially the inherent complexities of transitional winter precipitation.

Acknowledgments. PK and MO would like to acknowledge support by the National Science Foundation grant AGS-1841215. We thank the three anonymous reviewers for their detailed and thoughtful comments and suggestions that considerably improved the manuscript.

APPENDIX

Physical Interpretation of the Fully Polarimetric Radar Variables

The conventional dual-polarization radar variables are described fully in texts (e.g., Doviak and Zrnić 1993; Bringi and Chandrasekar 2001; Zhang 2016; Ryzhkov and Zrnić 2019) and in the literature (e.g., Zrnić and Ryzhkov 1999; Ryzhkov et al. 2005; Kumjian 2013a,b,c, 2018). In contrast, the fully polarimetric radar variables have received less attention. These quantities include the co-to-cross-polar correlation coefficients ρ_{xh} and ρ_{xv}, the cross-polar differential phase shifts

Φ_{XH} and Φ_{XV}, and the backscatter depolarization phase (δ_{cr}). Only a few studies have explored these correlation coefficients or phase shifts theoretically (Ryzhkov 2001; Moisseev et al. 2002; Melnikov 2006) or observationally (Ryzhkov et al. 2002; Melnikov et al. 2019). Here, we provide a conceptual description of LDR and ρ_{xh} with an emphasis on their physical interpretation. We do so by comparison with the more familiar co-polar quantities Z_{DR} and ρ_{hv}.

a. Z_{DR} and LDR

Z_{DR} is a measure of the difference in Z_H and Z_V (in logarithmic scale) and provides information on hydrometeor shapes (Seliga and Bringi 1976). For particles with more mass aligned in the horizontal than in the vertical, $Z_H > Z_V$, and thus $Z_{DR} > 0$ dB. For particles with more mass aligned in the vertical than in the horizontal, $Z_H < Z_V$, and thus $Z_{DR} < 0$ dB. (These rules no longer apply when particles are large compared to the radar wavelength.) This happens because near-field interactions (e.g., Kumjian 2018; Schrom and Kumjian 2018) between the tiny radiating volumes in a particle reinforce each other's internal electric field along the incident polarization direction, enhancing the backscattering magnitude, whereas they weaken each other's internal electric field in the direction orthogonal to the incident polarization (within the polarization plane), thereby reducing the backscattering magnitude. So, for a hydrometeor with its major axis in the horizontal, its backscatter is enhanced at horizontal polarization and reduced at vertical polarization (i.e., $Z_H > Z_V$). The strength of these near-field interactions increases with increasing relative permittivity ε_r, and/or increases in the mass density within the particle's bounding volume. Thus, for a given nonspherical particle shape, Z_{DR} is larger for liquid than for solid ice (e.g., ice pellet), which is larger than for sparsely packed ice (e.g., graupel or snow aggregate).

LDR is the difference in radar reflectivity factors between the cross-polarized component (i.e., transmit radiation at one polarization and receive at the orthogonal polarization) and the co-

polarized component (i.e., transmit and receive radiation at the same polarization). In order for a hydrometeor to depolarize the incident radiation, it must be (i) nonspherical, and (ii) have some asymmetry in its distribution of mass relative to the polarization axes. The second factor is required because particle symmetry about the polarization axes leads to cancellation of the near-field interactions that lead to the depolarization (e.g., Kumjian 2018). For example, spheroids can only depolarize the incident radiation their major axis does not align with the horizontal or vertical polarization directions. Irregular particles that have asymmetries, such as bulges or lobes, also lead to depolarization (e.g., Jiang et al. 2019). As with Z_{DR}, near-field interactions are stronger for larger ε_r and/or closer packing of the particle's mass. If there is no depolarization, the intrinsic LDR is $-\infty$ dB. However, in real radar systems, some of the co-polar signal is leaked into the cross-polar channel (i.e., there is cross-coupling). Thus, there is always a measured finite LDR signal (the "LDR limit"), which for KASPR is about -30 dB. The impacts of cross-coupling are described further below.

Z_{DR} and LDR are compared in Fig. c. In the top row, all particles are spheres, so $Z_{\mathrm{DR}} = 0$ dB and LDR $= -\infty$ dB, regardless of the particles' ε_r. In the second row, the particles are oblate spheroids perfectly oriented with their maximum dimension in the horizontal. Thus, Z_{DR} is maximized for the liquid particles (owing to the larger ε_r and thus larger near-field interactions) and decreases as you move right. LDR is still equal to $-\infty$ dB for each population in this row, because the particles are well oriented and have no asymmetries about the polarization axes. In the third row, the same oblate particles now have some slight dispersion of orientation angles. This leads to a reduction in Z_{DR} for all three populations, though Z_{DR} still decreases from left to right. Now, however, the canted hydrometeors depolarize the signal, so LDR $> -\infty$ dB for all populations, and decreases from left to right owing to the decreasing ε_r. Finally, the bottom row shows the same particle populations, but with further increased dispersion of orientation angles. This drives Z_{DR}

down closer to 0 dB, but increases LDR further. LDR is maximized for the liquid particles, and decreases as you move right towards the lower ε_r.

b. Conceptual Model for Co-polar and Co-to-cross-polar Correlation Coefficients

In practice, the radar probes a volume of the atmosphere using several pulses, between which the hydrometeors "reshuffle" their respective positions (e.g., Doviak and Zrnić 1993). Because the radar pulse volume is much wider than a single wavelength, the phases of the waves scattered by each hydrometeor add together in complicated ways, leading to constructive and destructive interference of these scattered waves (for an excellent visualization, see Fabry 2015). As such, at certain instances, we may think of certain hydrometeors being "invisible" to the radar (because their signals have destructively interfered with others and thus cancelled out), whereas others are "visible." From pulse to pulse, the reshuffling of hydrometeors means that the particles that are "visible" versus "invisible" will change. A sufficiently large number of pulses, then, will represent the ensemble average of particles in the sampling volume.

Consider a population of spherical particles of varying sizes within a radar sampling volume (Fig. A1). At the 3 times shown, different particles are "faded" out of view (i.e., do not contribute significantly to the overall received signal) because of reshuffling. Thus, Z_H and Z_V both fluctuate in time. However, because the particles are spheres, they scatter identically at horizontal and vertical polarizations, so Z_H and Z_V fluctuate identically. Thus, $Z_{\rm DR} = 0$ dB and is constant in time. Because there is no diversity of shapes or $Z_{\rm DR}$ in the sample volume (i.e., the Z_H and Z_V signals are perfectly correlated), the $\rho_{\rm hv}$ is unity. The same reasoning applies even if the particles were nonspherical but the same shape (i.e., some nonzero $Z_{\rm DR}$ but constant in time).

Figure A2 is the same concept, but with nonspherical particles of different shapes and sizes. Now, Z_H and Z_V fluctuate differently (i.e., they are not perfectly correlated) because the particles

fading "into" and "out of" view are of different shapes. This causes the Z_{DR} of each pulse to fluctuate, signaling a diversity of Z_{DR} within the sampling volume and thus a decrease in ρ_{hv}.

Now, we consider again the same population of nonspherical particles (Fig. A3). This time, we consider the co-polar Z_H, and the cross-polar component Z_{VH} (transmit H, receive V). Because all of our particles are spheroidal and perfectly aligned with their major axes along the polarization axes, there is no depolarization. Thus, LDR $= -\infty$ dB, and, intrinsically, $\rho_{\mathrm{xh}} = 0$. However, because of cross-coupling, there is a cross-polar signal (faded green line in the Z_H time series) that is perfectly correlated with the received co-polar signal because it comes entirely from the co-polar signal. Thus, the LDR is at the system limit and constant from pulse to pulse. Because there is no LDR diversity, $\rho_{\mathrm{xh}} = 1.0$. (In practice, $\rho_{\mathrm{xh}} < 1.0$ even for purely cross-coupled signals because the co-polar and cross-polar antenna beam patterns are not identical. As such, they illuminate different volumes of particles and thus have decorrelated signals (e.g., Moisseev et al. 2002). This is analogous to why ρ_{hv} is never identically equal to 1.0, though typically the horizontal and vertical polarization beam patterns are more closely matched than the co-polar and cross-polar beam patterns, so ρ_{hv} can be very close to 1.0 with high-quality antennas.)

Finally, we consider the same population yet again, but now the particles have some dispersion of orientation angles (Fig. A4). Because their major axes are not aligned with the polarization axes, depolarization occurs. The amount of depolarization depends on which particles are "in view" and how they are wobbling. Thus, LDR fluctuates from pulse to pulse (but never goes below the system limit). This "diversity of LDR" in from pulse to pulse indicates the co- and cross-polar signals are not perfectly correlated, so ρ_{xh} is low. In practice, it is reduced from its "background" value in non-depolarizing media (itself a result of cross-coupling and antenna imperfections described above).

c. Applications to Real Data

Figures 9d and 10d in the main text show data taken at vertical incidence. We see that LDR is somewhat larger in dry snow aggregates (~ -27 dB) just above the melting layer top than in the rain region (-30 dB), despite the much larger ε_r of liquid. This is for two reasons. First, aggregates are not spheroids, better represented by prolate tri-axial ellipsoids (e.g., Dunnavan et al. 2019). In contrast, rain is approximately spheroidal, and thus appears isotropic when viewed from below owing to their vertically oriented (on average) rotational symmetry axis. Second, snow aggregates have a larger dispersion of orientation angles than raindrops (e.g., Dunnavan 2020). The measured ρ_{xh} in rain is greater than in aggregates because the intrinsic LDR is lower in rain, and thus cross-coupling dominates the signal and leads to a positive bias (e.g., Moisseev et al. 2002; Melnikov 2006).

In the melting layer, LDR is strongly enhanced and ρ_{xh} decreased. These are both explained by the highly nonspherical and chaotically oriented particles acquiring liquid (and thus a significant increase in their ε_r). Analogously to the melting layer signature in ρ_{hv}, the increase in ε_r augments the near-field interactions and thus the signals in all polarimetric radar quantities. Ryzhkov et al. (2002) attribute locally lower values of ρ_{xh} in the melting layer to increased snowflake wobbling. However, dry snow also wobbles, but exhibits larger ρ_{xh}. Thus, increased ε_r of particles beginning to melt exaggerates the diversity of LDR (much like ρ_{hv} minima deepen when particles are wet). Also, diversity of δ_{cr} for wet, nonspherical, non-Rayleigh particles lowers ρ_{xh}, much like diversity of δ decreases ρ_{hv}.

From the rain region to the refreezing layer (RFL), we observe an LDR increase and ρ_{xh} decrease, despite the decreasing particle ε_r as they undergo freezing. Here, increases in particle wobbling and/or increases in particle shape irregularities/asymmetries must be occurring. Also,

note both LDR and ρ_{xh} in snow aggregates and in the RFL are similar. However, larger near-field interactions are expected for solid ice particles (ice pellets) compared to fluffier snow aggregates or graupel. This indicates particles in the RFL feature fewer asymmetries/irregular shapes and/or less wobbling than aggregates (but more than in rain). In other words, the ice pellets or refreezing particles are not spheroids, and have some asymmetries.

References

Alkezweeny, A., 1969: Freezing of supercooled water droplets due to collision. *J. Appl. Meteor.*, **8**, 994–995.

Aydin, K., and T. M. Walsh, 1999: Millimeter wave scattering from spatial and planar bullet rosettes. *IEEE Trans. Geosci. Remote Sens.*, **37**, 1138–1150.

Bailey, M. P., and J. Hallett, 2009: A comprehensive habit diagram for atmospheric ice crystals: Confirmation from the laboratory, AIRS II, and other field studies. *J. Atmos. Sci.*, **66**, 2888–2899.

Benjamin, S. G., and Coauthors, 2016: A North American hourly assimilation and model forecast cycle: The Rapid Refresh. *Mon. Wea. Rev.*, **144**, 1669–1694.

Bernstein, B., T. Omeron, M. Politovich, and F. McDonough, 1998: Surface weather features associated with freezing precipitation and severe inflight aircraft icing. *Atmos. Res.*, **46**, 57–73.

Bigg, E. K., 1953: The formation of atmospheric ice crystals by the freezing of droplets. *Quart. J. Roy. Meteor. Soc.*, **79**, 510–519.

Black, A. W., and T. L. Mote, 2015: Effects of winter precipitation on automobile collisions, injuries, and fatalities in the united states. *J. Transp. Geogr.*, **48**, 165–175.

Bringi, V. N., and V. Chandrasekar, 2001: *Polarimetric Doppler Weather Radar*. 1st ed., Cambridge University Press, 636 pp.

Bukovčić, P., D. Zrnić, and G. Zhang, 2017: Winter precipitation liquid-ice phase transitions revealed with polarimetric radar and 2dvd observations in central Oklahoma. *J. Appl. Meteor. Climatol.*, **56**, 1345–1363.

Call, D. A., 2010: Changes in ice storm impacts over time: 1886–2000. *Wea. Clim. Soc.*, **2**, 23–35.

Chisnell, R. F., and J. Latham, 1976: Ice particle multiplication in cumulus clouds. *Quart. J. Roy. Meteor. Soc.*, **102**, 133–156.

Cortinas, J. V., B. C. Bernstein, C. C. Robbins, and J. W. Strapp, 2004: An analysis of freezing rain, freezing drizzle, and ice pellets across the United States and Canada: 1976-90. *Wea. Forecasting*, **19**, 377–390.

Czys, R., 1989: Ice initiation by collision-freezing in warm-based nuclei. *J. Appl. Meteor.*, **28**, 1098–1104.

Doviak, R. J., and D. S. Zrnić, 1993: *Doppler Radar and Weather Observations*. 2nd ed., Academic Press, 562 pp.

Dunnavan, E. L., 2020: How snow aggregate shape and orientation variability affects fall speed and self-collection rates. *J. Atmos. Sci.*, **in review**.

Dunnavan, E. L., Z. Jiang, J. Y. Harrington, J. Verlinde, K. Fitch, and T. J. Garrett, 2019: The shape and density evolution of snow aggregates. *J. Atmos. Sci.*, **76**, 3919–3940.

Fabry, F., 2015: *Radar Meteorology: Principles and Practice*. 1st ed., Cambridge University Press, 256 pp.

Fukuta, N., 1975: A study of the mechanism of contact ice nucleation. *J. Atmos. Sci.*, **32**, 1597–1603.

Gibson, S. R., and R. E. Stewart, 2007: Observations of ice pellets during a winter storm. *Atmos. Res.*, **85**, 64–76.

Hobbs, P., 1965: The aggregation of ice particles in clouds and fogs at low temperatures. *J. Atmos. Sci.*, **22**, 296–300.

Houze, R. A., and S. Medina, 2005: Turbulence as a mechanism for orographic precipitation enhancement. *J. Atmos. Sci.*, **62**, 3599–3623.

Jiang, Z., M. R. Kumjian, R. S. Schrom, I. M. Giammanco, T. Brown-Giammanco, R. Maiden, and A. Heymsfield, 2019: Comparisons of electromagnetic scattering properties of real hailstones and spheroids. *J. Appl. Meteor. Climatol.*, **58**, 93–112.

Jones, K. F., A. C. Ramsay, and J. N. Lott, 2004: Icing severity in the December 2002 freezing-rain storm from ASOS data. *Mon. Wea. Rev.*, **132**, 1630–1644.

Kajikawa, M., 1972: Measurement of falling velocity of individual snow crystals. *J. Meteor. Soc. Japan*, **50**, 577–583.

Kanji, Z. A., L. A. Ladino, H. Wex, Y. Boose, M. Burkert-Kohn, D. Cziczo, and M. Krämer, 2017: Overview of ice nucleating particles. *"Meteor. Monogr."*, **58**, 1–33.

Koenig, R. L., 1965: Drop freezing through drop breakup. *J. Atmos. Sci.*, **22**, 448–451.

Kollias, P., and B. Albrecht, 2005: Why the melting layer radar refelctivity is not bright at 94 GHz. *Geophys. Res. Let.*, **32**, L24 818.

Kollias, P., N. Bharadwaj, K. Widener, I. Jo, and K. Johnson, 2014: Scanning ARM cloud radars. Part I: Operational sampling strategies. *J. Atmos. Oceanic Technol.*, **31**, 569–582.

Kumjian, M. R., 2013a: Principles and applications of dual-polarization weather radar. Part I: Description of the polarimetric radar variables. *J. Operational Meteor.*, **1**, 226–242.

Kumjian, M. R., 2013b: Principles and applications of dual-polarization weather radar. Part II: Warm and cold season applications. *J. Operational Meteor.*, **1**, 243–264.

Kumjian, M. R., 2013c: Principles and applications of dual-polarization weather radar. Part III: Artifacts. *J. Operational Meteor.*, **1**, 265–274.

Kumjian, M. R., 2018: Weather radars. *Remote Sensing of Clouds and Precipitation*, C. Andronache, Ed., Springer-Verlag, 15–63.

Kumjian, M. R., S. M. Ganson, and A. V. Ryzhkov, 2012: Raindrop freezing in deep convective updrafts: A microphysical and polarimetric model. *J. Atmos. Sci.*, **69**, 3471–3490.

Kumjian, M. R., and K. A. Lombardo, 2017: Insights into the evolving microphysical and kinematic structure of northeastern u.s. winter storms from dual-polarization doppler radar. *Mon. Wea. Rev.*, **145**, 1033–1061.

Kumjian, M. R., and O. P. Prat, 2014: The impact of raindrop collisional processes on the polarimetric radar variables. *J. Atmos. Sci.*, **71**, 3052–3067.

Kumjian, M. R., and A. V. Ryzhkov, 2010: The impact of evaporation on polarimetric characteristics of rain: Theoretical model and practical implications. *J. Appl. Meteor. Climatol.*, **49**, 1247–1267.

Kumjian, M. R., and A. V. Ryzhkov, 2012: The impact of size sorting on the polarimetric radar variables. *J. Atmos. Sci.*, **69**, 2042–2060.

Kumjian, M. R., A. V. Ryzhkov, H. D. Reeves, and T. J. Schuur, 2013: A dual-polarization radar signature of hydrometeor refreezing in winter storms. *J. Appl. Meteor. Climatol.*, **52**, 2549–2566.

Kumjian, M. R., and A. D. Schenkman, 2014: The curious case of ice pellets over Middle Tennessee on 1 March 2014. *J. Operational Meteor.*, **2**, 209–213.

Lawson, R. P., S. Woods, and H. Morrison, 2015: The microphysics of ice and precipitation development in tropical cumulus clouds. *J. Atmos. Sci.*, **72**, 2429–2445.

Li, H., and D. Moisseev, 2020: Two layers of melting ice particles within a single radar bright band: Interpretation and implications. *Geophys. Res. Let.*, **in press**.

Matrosov, S. Y., 1991: Theoretical study of radar polarization parameters obtained from cirrus clouds. *J. Atmos. Sci.*, **48**, 1062–1070.

Matrosov, S. Y., 2005: Attenuation-based estimates of rainfall rates aloft with vertically pointing Ka-band radars. *J. Atmos. Oceanic Technol.*, **22**, 43–54.

Matrosov, S. Y., R. A. Kropfli, R. F. Reinking, and B. E. Martner, 1999: Prospects for measuring rainfall using propagation differential phase in X- and Ka-radar bands. *J. Appl. Meteor.*, **38**, 766–776.

Matrosov, S. Y., R. F. Reinking, R. A. Kropfli, B. E. Martner, and B. W. Bartram, 2001: On the use of radar depolarization ratios for estimating shapes of ice hydrometeors in winter clouds. *J. Appl. Meteor.*, **40**, 479–490.

Melnikov, V., 2006: One-lag estimators for cross-polarization measurements. *J. Atmos. Oceanic Technol.*, **23**, 915–926.

729 Melnikov, V., D. Zrnić, M. Weber, A. O. Fierro, and D. R. MacGorman, 2019: Electrified cloud
730 areas observed in the SHV and LDR radar modes. *J. Atmos. Oceanic Technol.*, **36**, 151–159.

731 Moisseev, D. N., C. Unal, H. Russchenberg, and L. Ligthart, 2002: Improved polarimetric calibra-
732 tion for atmospheric radars. *J. Atmos. Oceanic Technol.*, **19**, 1968–1977.

733 Nagumo, N., A. Adachi, and H. Yamauchi, 2019: Geometrical properties of hydrometeors during
734 the refreezing process and their effects on dual-polarized radar signals. *Mon. Wea. Rev.*, **147**,
735 1753–1768.

736 Nagumo, N., and Y. Fujiyoshi, 2015: Microphysical properties of slow-falling and fast-falling ice
737 pellets formed by freezing associated with evaporative cooling. *Mon. Wea. Rev.*, **143**, 4376–
738 4392.

739 Oue, M., P. Kollias, A. V. Ryzhkov, and E. P. Luke, 2018: Toward exploring the synergy between
740 cloud radar polarimetry and Doppler spectral analysis in deep cold precipitating systems in the
741 Arctic. *J. Geophys. Res. Atmos.*, **123**, 2797–2815.

742 Oue, M., M. R. Kumjian, Y. Lu, J. Verlinde, K. Aydin, and E. E. Clothiaux, 2015: Linear depolar-
743 ization ratios of columnar ice crystals in a deep precipitating system over the Arctic observed
744 by zenith-pointing Ka-band Doppler radar. *J. Appl. Meteor. Climatol.*, **54**, 1060–1068.

745 Pitter, R. L., and H. R. Pruppacher, 1973: A wind tunnel investigation of freezing of small water
746 drops falling at terminal velocity in air. *Quart. J. Roy. Meteor. Soc.*, **99**, 540–550.

747 Pruppacher, H. R., and J. D. Klett, 1997: *Microphysics of Clouds and Precipitation*. 2nd ed.,
748 Kluwer Academic Publishers, 954 pp.

749 Ralph, F. M., and Coauthors, 2005: Improving short-term (0-48 h) cool-season quantitative pre-
750 cipitation forecasting. Recommendations froma USWRP Workshop. *Bull. Amer. Meteor. Soc.*,
751 **86**, 1619–1632.

752 Rauber, R. M., L. S. Olthoff, M. K. Ramamurthy, D. Miller, and K. E. Kunkel, 2001: A synoptic
753 weather pattern and sounding-based climatology of freezing precipitation in the United States
754 east of the Rocky Mountains. *J. Appl. Meteor.*, **40**, 1724–1747.

755 Reinking, R. F., S. Y. Matrosov, L. A. Kropfli, and B. W. Bartram, 2002: Evaluation of a slant
756 quasi-linear radar polarization state for distinguishing drizzle droplets, pristine ice crystals, and
757 less regular ice particles. *J. Atmos. Oceanic Technol.*, **19**, 296–321.

758 Ryzhkov, A. V., 2001: Interpretation of polarimetric radar covariance matrix for meteorological
759 scatterers. Theoretical analysis. *J. Atmos. Oceanic Technol.*, **18**, 315–328.

760 Ryzhkov, A. V., T. J. Schuur, D. W. Burgess, P. L. Heinselman, S. E. Giangrande, and D. S. Zrnić,
761 2005: The Joint Polarization Experiment: Polarimetric rainfall measurements and hydrometeor
762 classification. *Bull. Amer. Meteor. Soc.*, **86**, 809–824.

763 Ryzhkov, A. V., P. Zhang, H. D. Reeves, M. R. Kumjian, T. Tschallener, S. Trömel, and C. Simmer,
764 2016: Quasi-vertical profiles: a new way to look at polarimetric radar data. *J. Atmos. Oceanic*
765 *Technol.*, **33**, 551–562.

766 Ryzhkov, A. V., and D. S. Zrnić, 2019: *Radar Polarimetry for Weather Observations*. 1st ed.,
767 Springer, 486 pp.

768 Ryzhkov, A. V., D. S. Zrnić, J. C. Hubbert, V. N. Bringi, J. Vivekanandan, and E. A. Brandes, 2002:
769 Polarimetric radar observations and interpretation of co-cross-polar correlation coefficients. *J.*
770 *Atmos. Oceanic Technol.*, **19**, 340–354.

Schrom, R. S., and M. R. Kumjian, 2018: Bulk-density representations of branched planar ice crystals: Errors in the polarimetric radar variables. *J. Appl. Meteor. Climatol.*, **57**, 333–346.

Seliga, T. A., and V. N. Bringi, 1976: Potential use of radar differential reflectivity measurements at orthogonal polarizations for measuring precipitation. *J. Appl. Meteor.*, **15**, 69–76.

Shaw, R. A., W. C. Reade, L. R. Collins, and J. Verlinde, 1999: Preferential concentration of cloud droplets by turbulence: Effects on the early evolution of cumulus cloud droplet spectra. *J. Atmos. Sci.*, **55**, 1965–1976.

Stewart, R. E., and R. W. Crawford, 1995: Some characteristics of the precipitation formed within winter storms over eastern Newfoundland. *Atmos. Res.*, **36**, 17–37.

Stewart, R. E., J. Thériault, and W. Henson, 2015: On the characteristics of and processes producing winter precipitation types near 0 °c. *Bull. Amer. Meteor. Soc.*, **96**, 623–639.

Szyrmer, W., and I. Zawadzki, 1999: Modeling of the melting layer. Part I: Dynamics and microphysics. *J. Atmos. Sci.*, **56**, 3573–3592.

Tobin, D. M., and M. R. Kumjian, 2017: Polarimetric radar and surface-based precipitation-type observations of ice pellet to freezing rain transitions. *Wea. Forecasting*, **32**, 2065–2082.

Tobin, D. M., M. R. Kumjian, and A. W. Black, 2020: Effects of precipitation type on crash relative risk estimates in Kansas. *Accident Anal. Prev.*, **submitted**.

Vali, G., 1994: Freezing rate due to heterogeneous nucleation. *J. Atmos. Sci.*, **51**, 1843–1856.

Van Den Broeke, M. S., D. M. Tobin, and M. R. Kumjian, 2016: Polarimetric radar observations of precipitation type and rate from the 2-3 March 2014 winter storm in Oklahoma and Arkansas. *Wea. Forecasting*, **31**, 1179–1196.

Xie, X., R. Evaristo, S. Troemel, P. Saavedra, C. Simmer, and A. V. Ryzhkov, 2016: Radar observation of evaporation and implications for quantitative precipitation and cooling rate estimation. *J. Atmos. Oceanic Technol.*, **33**, 1779–1792.

Yang, F., W. H. Cantrell, A. B. Kostinski, R. A. Shaw, and A. M. Vogelmann, 2019: Is contact nucleation caused by pressure perturbation? *"Atmosphere"*, **11**, 1–16.

Yang, F., O. Cruikshank, W. He, A. Kostinski, and R. A. Shaw, 2018: Nonthermal ice nucleation observed at distorted contact lines of supercooled water drops. *Phys. Rev. E.*, **97**, 023 103.

Zawadzki, I., W. Szyrmer, C. Bell, and F. Fabry, 2005: Modeling of the melting layer. Part III: The density effect. *J. Atmos. Sci.*, **62**, 3705–3723.

Zerr, R. J., 1997: Freezing rain: an observational and theoretical study. *J. Appl. Meteor.*, **36**, 1647–1661.

Zhang, G., 2016: *Weather Radar Polarimetry*. 1st ed., CRC Press, 322 pp.

Zrnić, D. S., and A. V. Ryzhkov, 1999: Polarimetry for weather surveillance radars. *Bull. Amer. Meteor. Soc.*, **80**, 389–406.

LIST OF TABLES

TABLE 1. KASPR technical specifications

Specification	Value
Frequency	35.29 GHz
Wavelength	8.5 mm
Peak Transmit Power	2.2 kW
Pulse Repetition Frequency	staggered; maximum 15 KHz
Range Resolution	Selectable; 15 m to 200 m
Transmit Polarization	Pulse-to-pulse switchable H/V
Receiver Polarization	Simultaneous H/V
Antenna Diameter	1.8 m
Antenna Beamwidth	0.32°
Antenna Gain	53.3 dBi
Cross-polarization isolation	-27 dB

LIST OF FIGURES

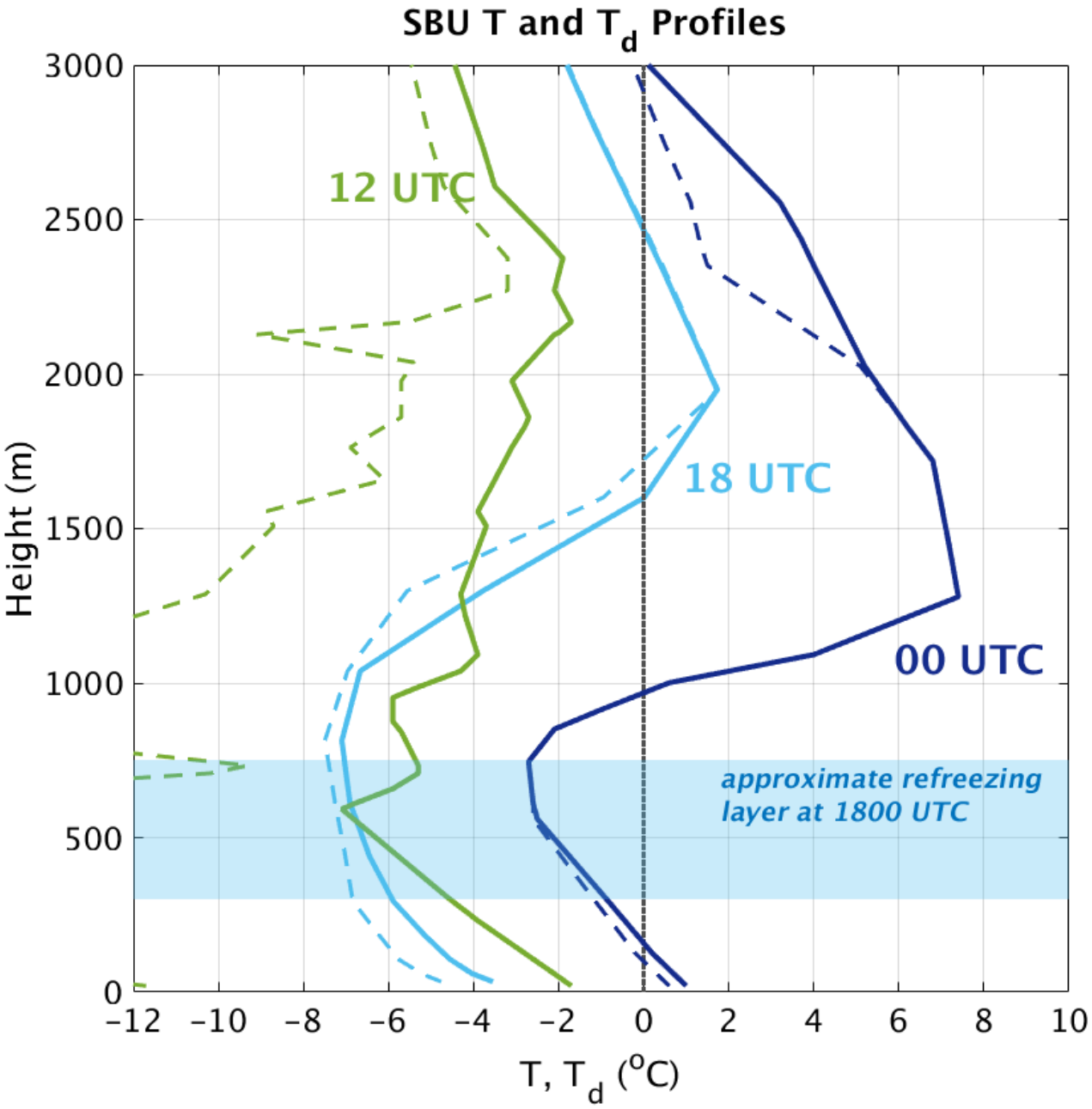

894 FIG. 1. Vertical temperature (T, solid) and dewpoint temperature (T_d, dashed) profiles over Stony Brook
895 University (SBU) on central Long Island at 12 UTC 12 February 2019 (green), 18 UTC 12 February 2019
896 (cyan), and 00 UTC 13 February 2019 (dark blue). The 12 and 00 UTC profiles are from observed soundings in
897 Upton, NY (KOKX), whereas the 18 UTC profiles are from the RAP model analysis at the grid box closest to
898 SBU. The shaded cyan region represents the radar-indicated refreezing layer at about 1800 UTC.

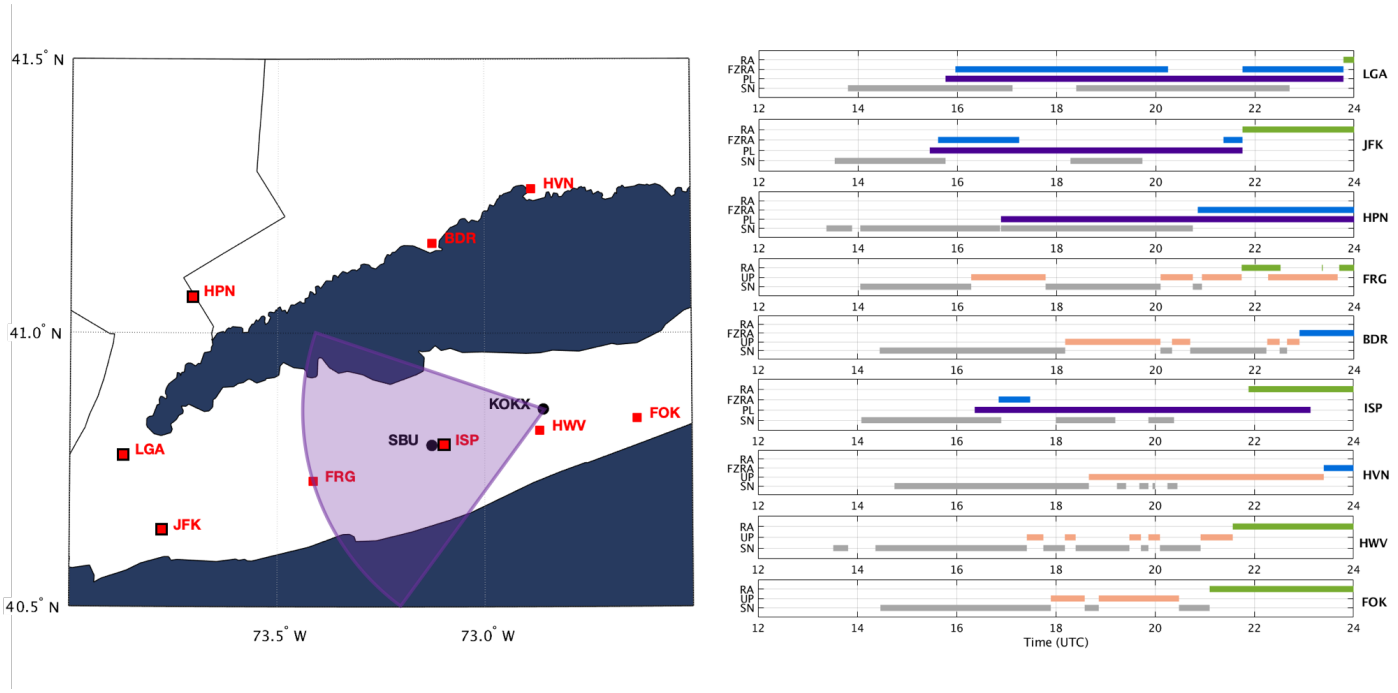

899 FIG. 2. Overview of precipitation type observed throughout the event. The left panel shows the map of the
900 observation stations of interest, with ASOS/AWOS stations in red, and the locations of Stony Brook University
901 (SBU) and KOKX in black. The black frame around the red markers indicates those observing stations are
902 human augmented. The purple wedge shows the ranges and azimuths included in the range-azimuth-defined
903 QVP in Fig. 3. The right panel shows the observed precipitation types at each station, with top-to-bottom order
904 indicating geographic location west to east. The bars show precipitation occurrences, with gray for snow (SN),
905 salmon for unknown precipitation type (UP), purple for ice pellets (PL), blue for freezing rain (FZRA), and
906 green for rain (RA).

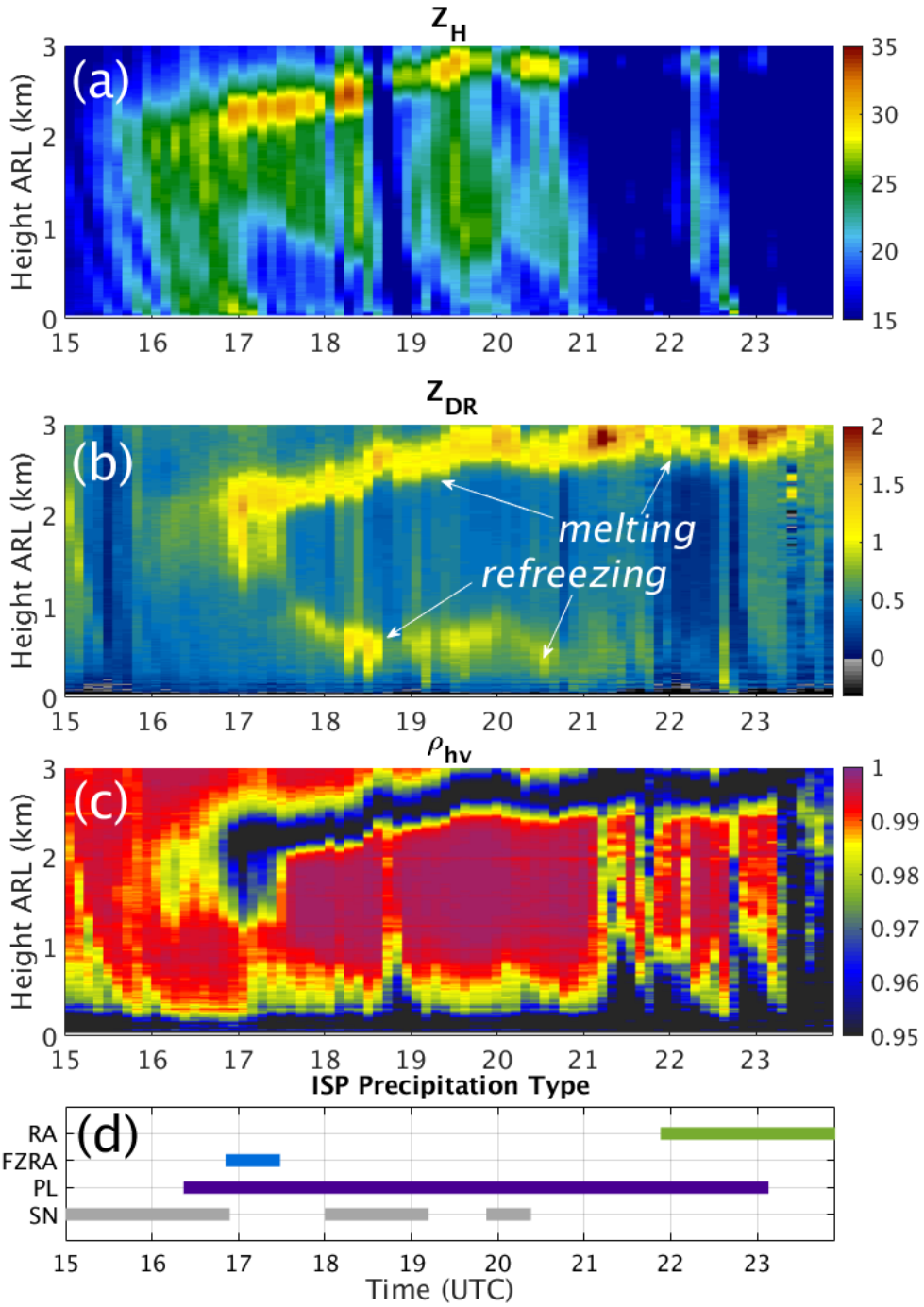

907 FIG. 3. Range-azimuth-defined quasi-vertical profile (raQVP) from KOKX, constructed with data from the
908 purple wedge in Fig. 2. (a) Z_H, (b) Z_{DR}, (c) ρ_{hv}. Panel (d) shows the time series of precipitation types from
909 the nearby Islip airport human-augmented observing station (ISP). Gray, purple, blue, and green bars represent
910 snow (SN), ice pellets (PL), freezing rain (FZRA), and rain (RA), respectively.

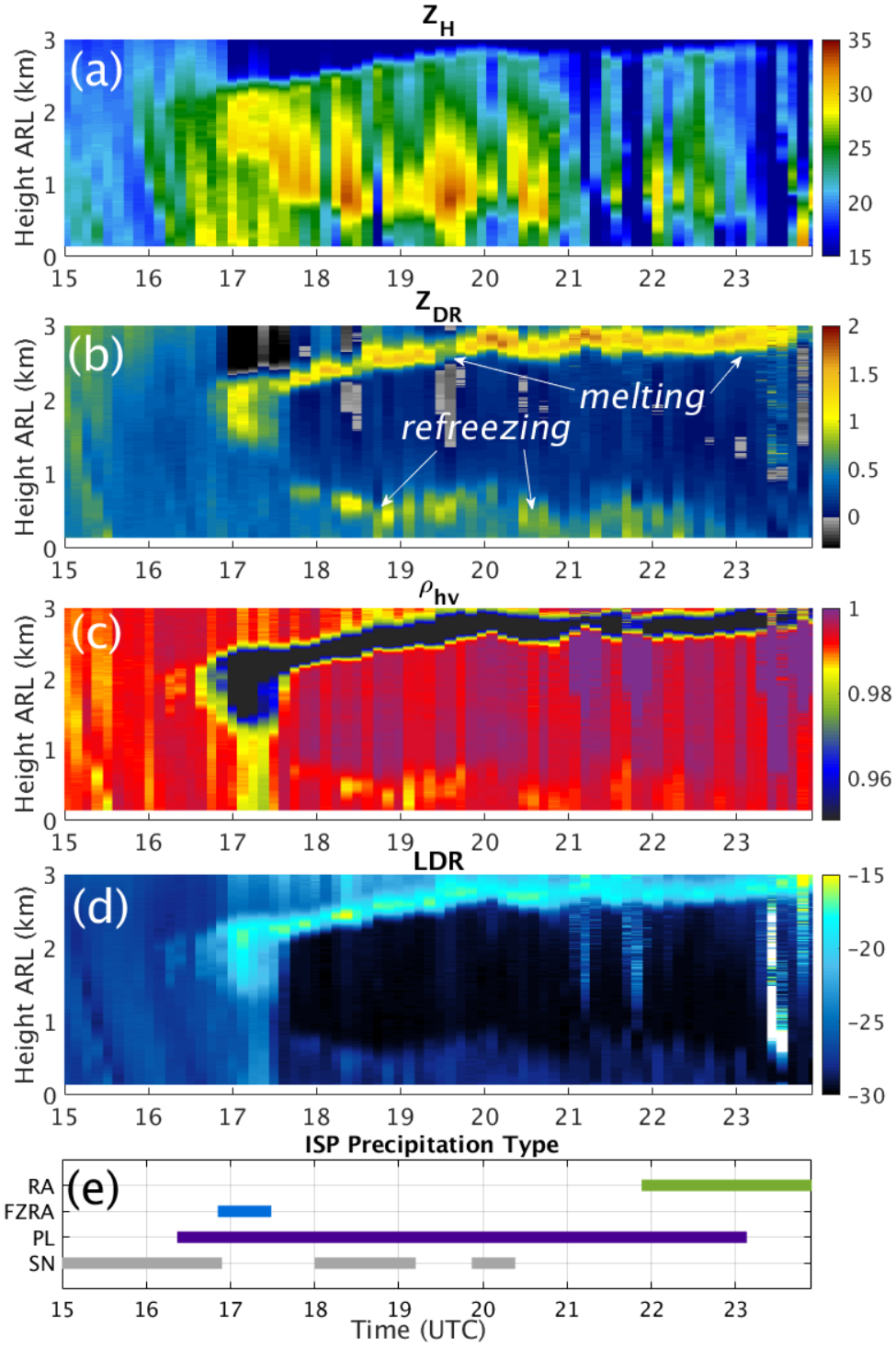

FIG. 4. Quasi-vertical profile (QVP) from KASPR: (a) Z_H, (b) Z_{DR}, (c) ρ_{hv}, and (d) LDR. Panel (e) shows the time series of precipitation types from the nearby Islip airport human-augmented observing station (ISP). Gray, purple, blue, and green bars represent snow (SN), ice pellets (PL), freezing rain (FZRA), and rain (RA), respectively.

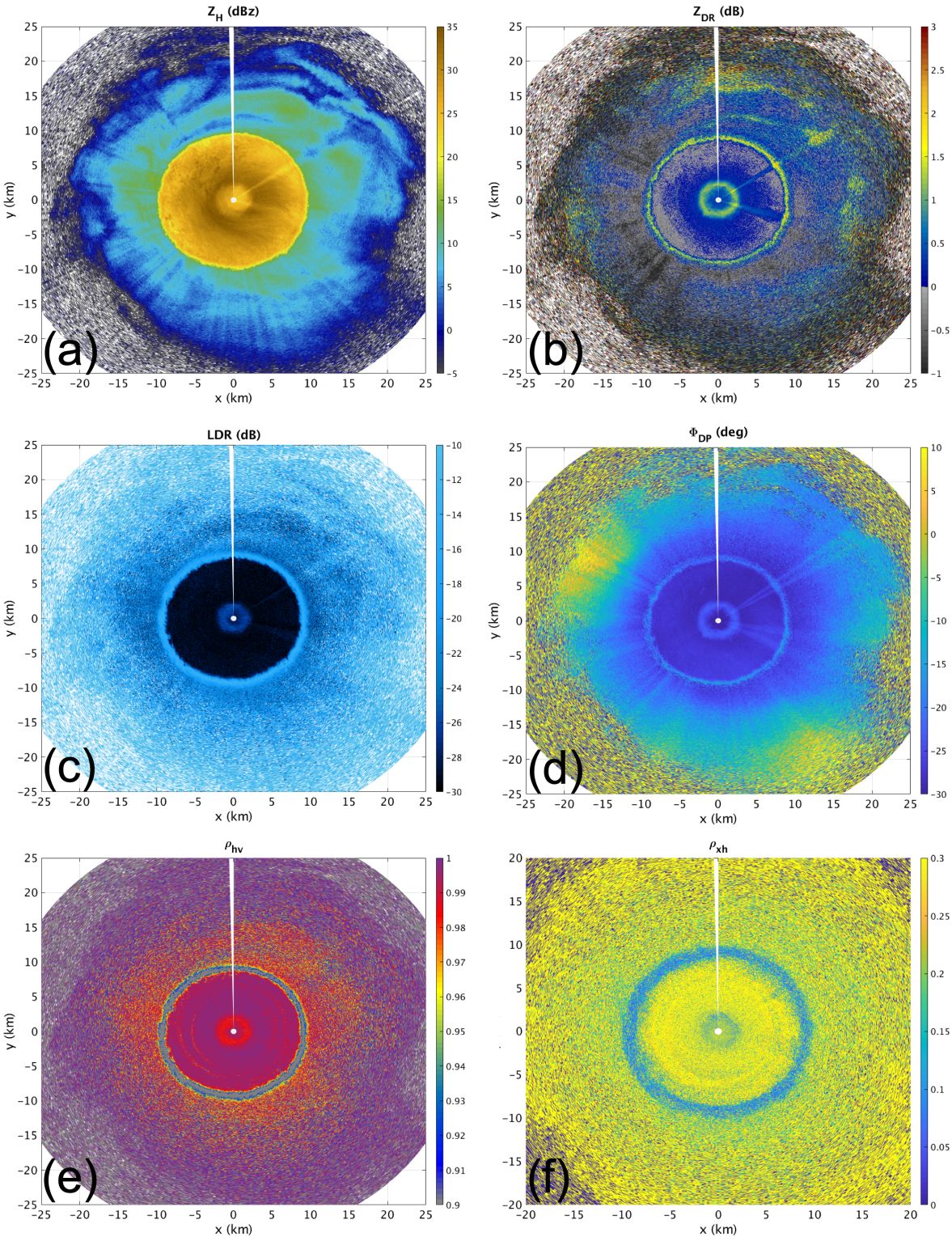

915 FIG. 5. Fields of (a) Z_H, (b) Z_{DR}, (c) LDR, (d) Φ_{DP}, (e) ρ_{hv}, and (f) ρ_{xh} taken at 15° elevation angle at 1817
916 UTC by KASPR.

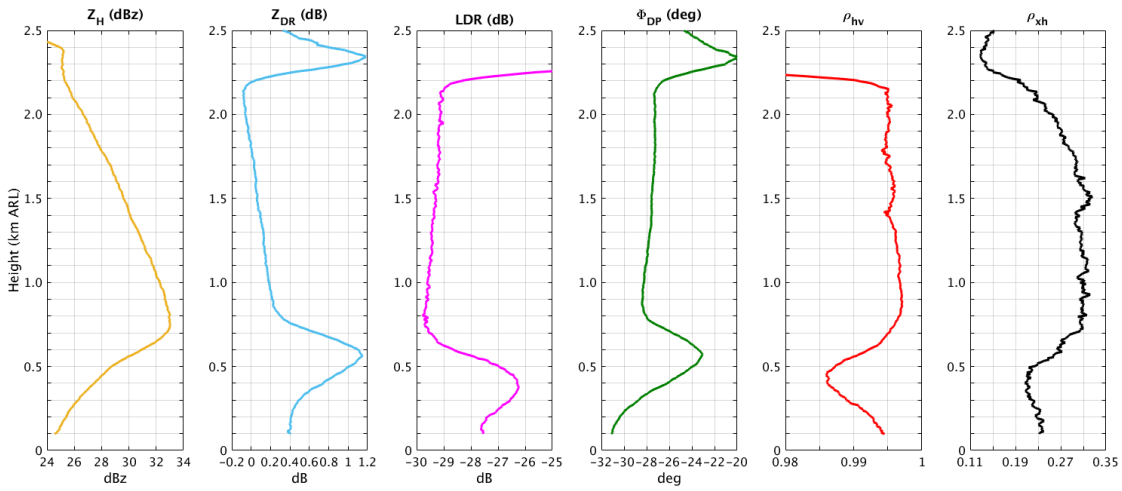

FIG. 6. QVPs from the PPIs shown in Fig. 5.

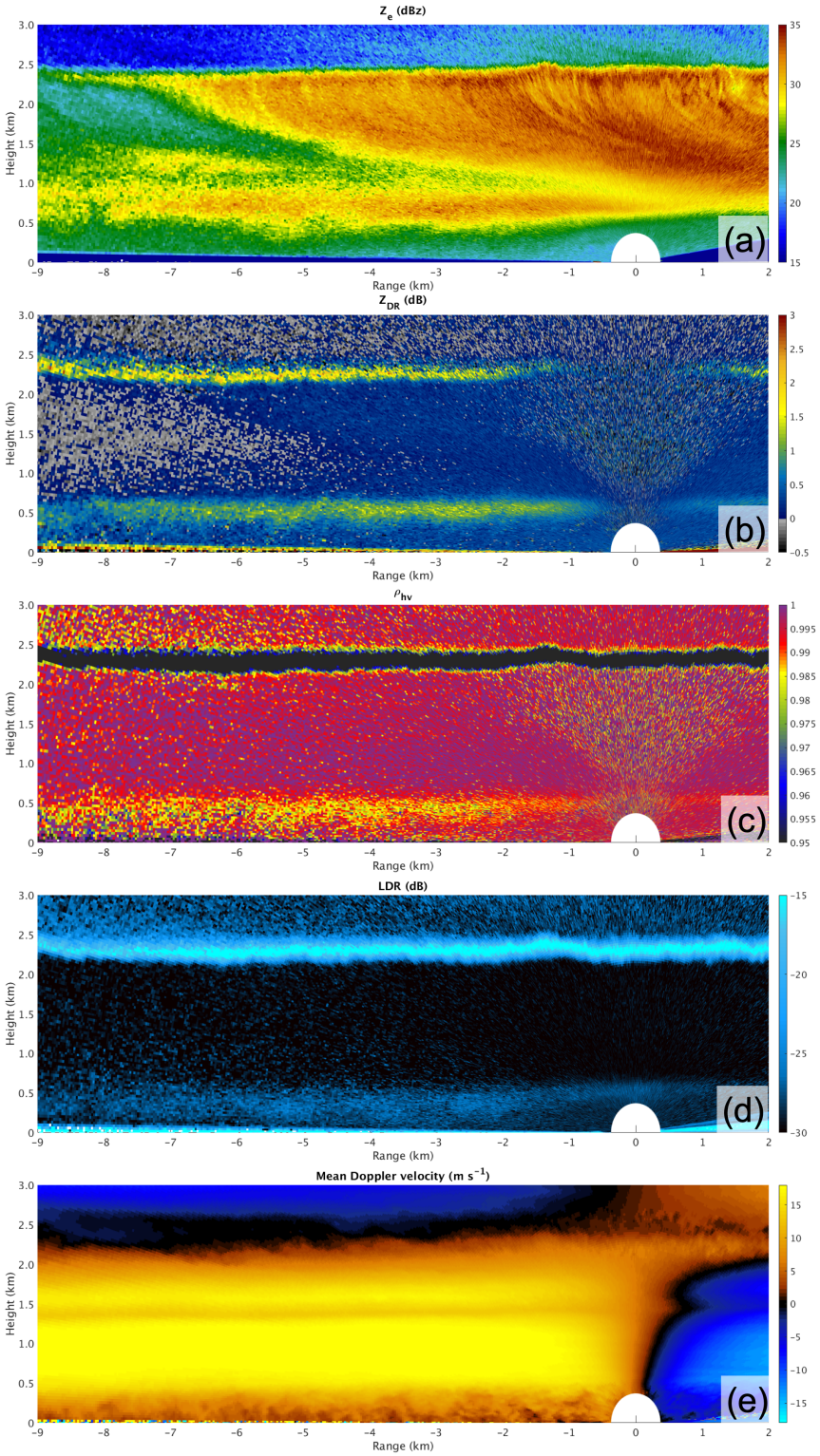

FIG. 7. RHI scans from 1813 UTC. Fields shown are (a) Z_H, (b) Z_{DR}, (c) ρ_{hv}, (d) LDR, and (e) mean Doppler velocity. Data taken along the azimuth 135°.

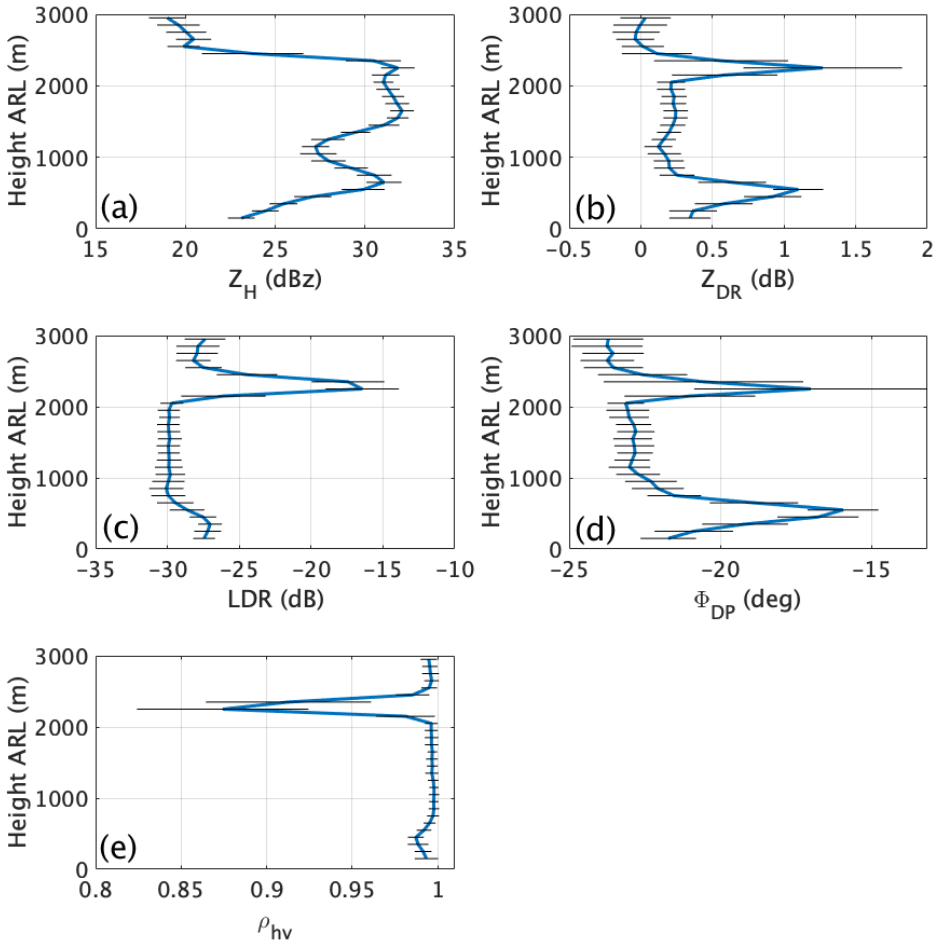

FIG. 8. Average vertical profiles extracted from RHI scans from 1813 UTC (solid blue lines) with ± 1 standard deviation error bars included. Vertical profiles are extracted from the range interval -4 to -3 km in the hemispheric RHI scan from Fig. 7.

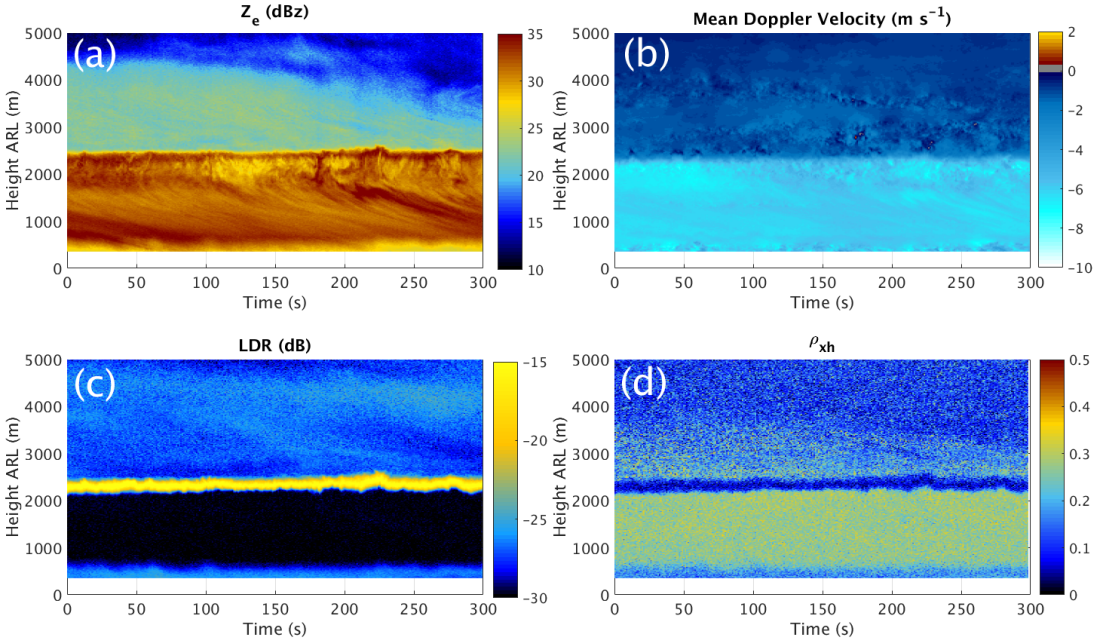

FIG. 9. Time-height depictions from KASPR vertically pointing mode showing (a) Z_e, (b) mean Doppler velocity, (c) LDR, and (d), ρ_{xh}. Data collected over a five-minute period beginning at 1820 UTC.

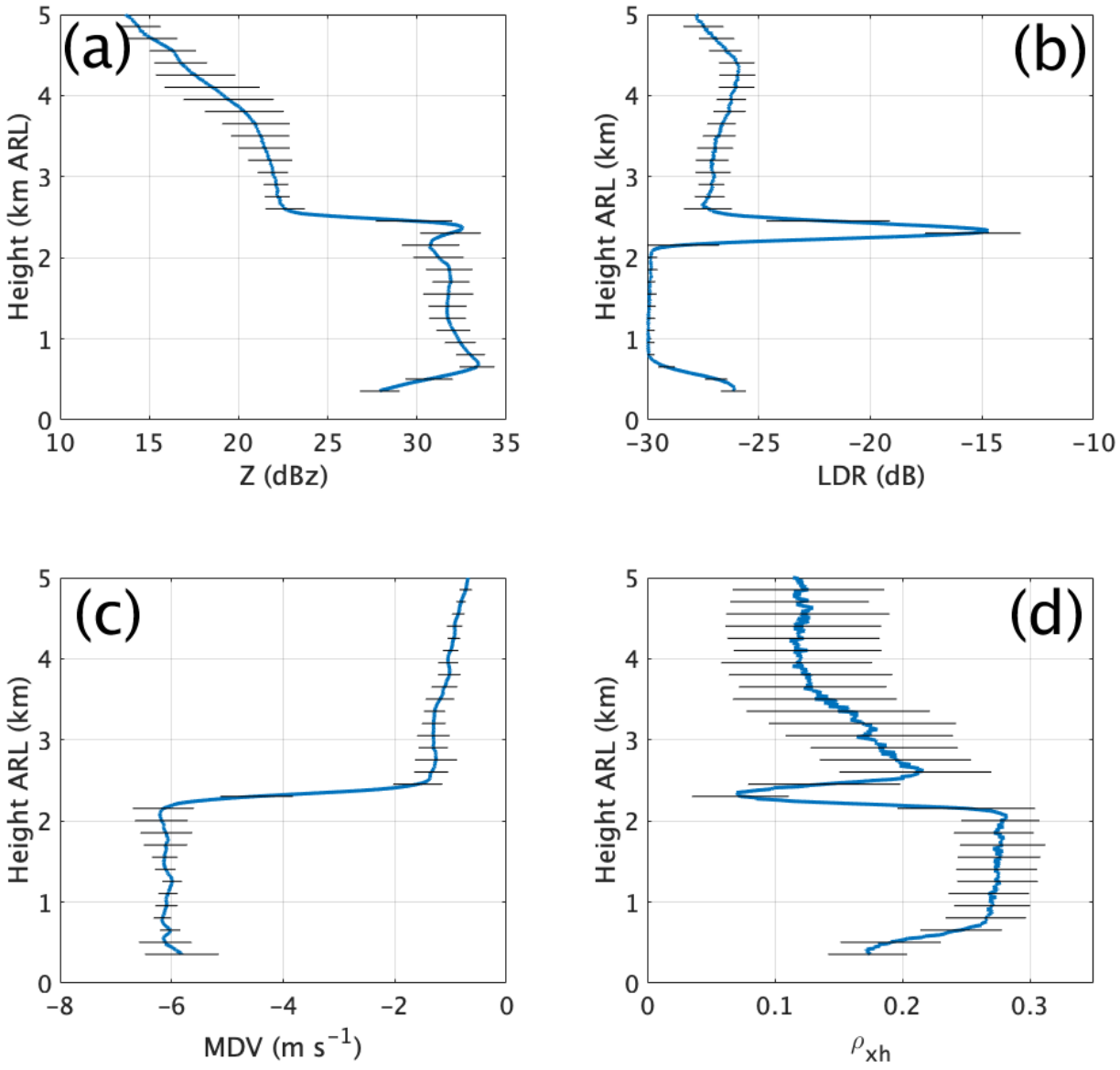

924 FIG. 10. Average vertical profiles from the vertically pointing KASPR scans shown in Fig. 9. Solid lines are
925 the average, with ± 1 standard deviation error bars overlaid. Data are averaged starting at 1820 UTC.

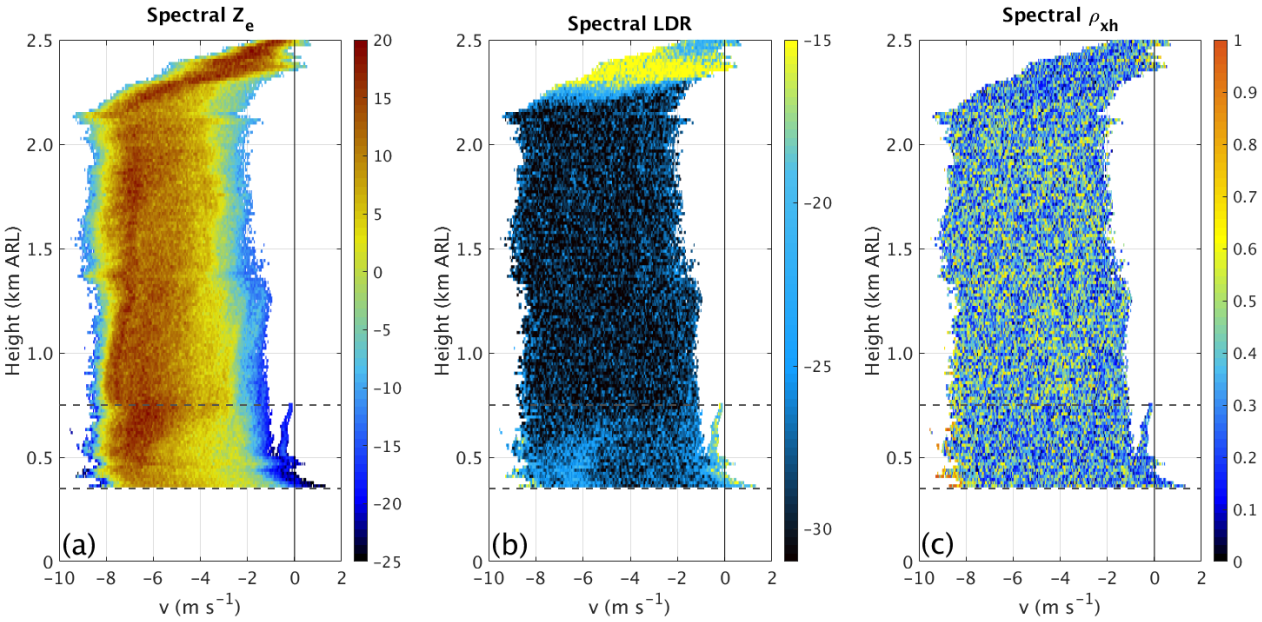

FIG. 11. 1-second spectral data from a vertically pointing KASPR scan at 1822:57 UTC. (a) spectral Z_e, (b) spectral LDR, (c) spectral ρ_{xh}. The horizontal dashed lines show the domain featured in Fig. 15.

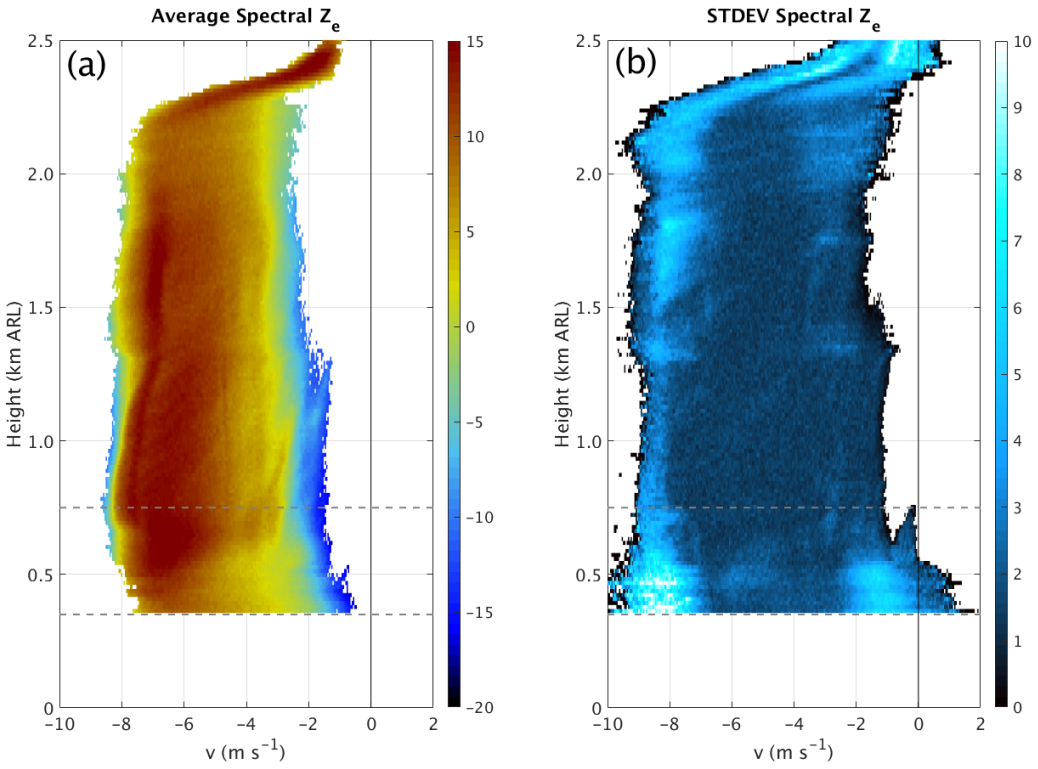

928 FIG. 12. 30-second average spectragraph of (a) spectral Z_e, and (b) its standard deviation, both in dB, shaded
929 according to the colorbars. The horizontal dashed lines represent the domain shown in Fig. 15, where refreezing
930 occurs. Data are averaged from 1821:57 to 1822:27 UTC.

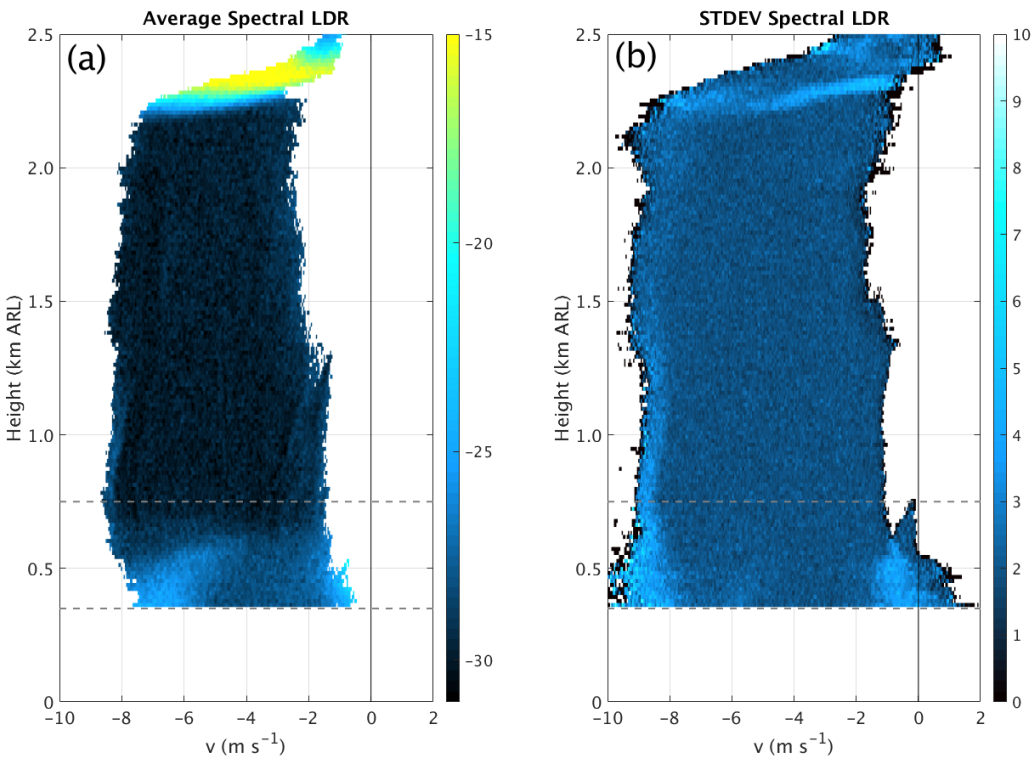

931 FIG. 13. 30-second average spectragraph of (a) spectral LDR, and (b) its standard deviation, both in dB,
932 shaded according to the colorbars. The horizontal dashed lines represent the domain shown in Fig. 15, where
933 refreezing occurs. Data are averaged from 1821:57 to 1822:27 UTC.

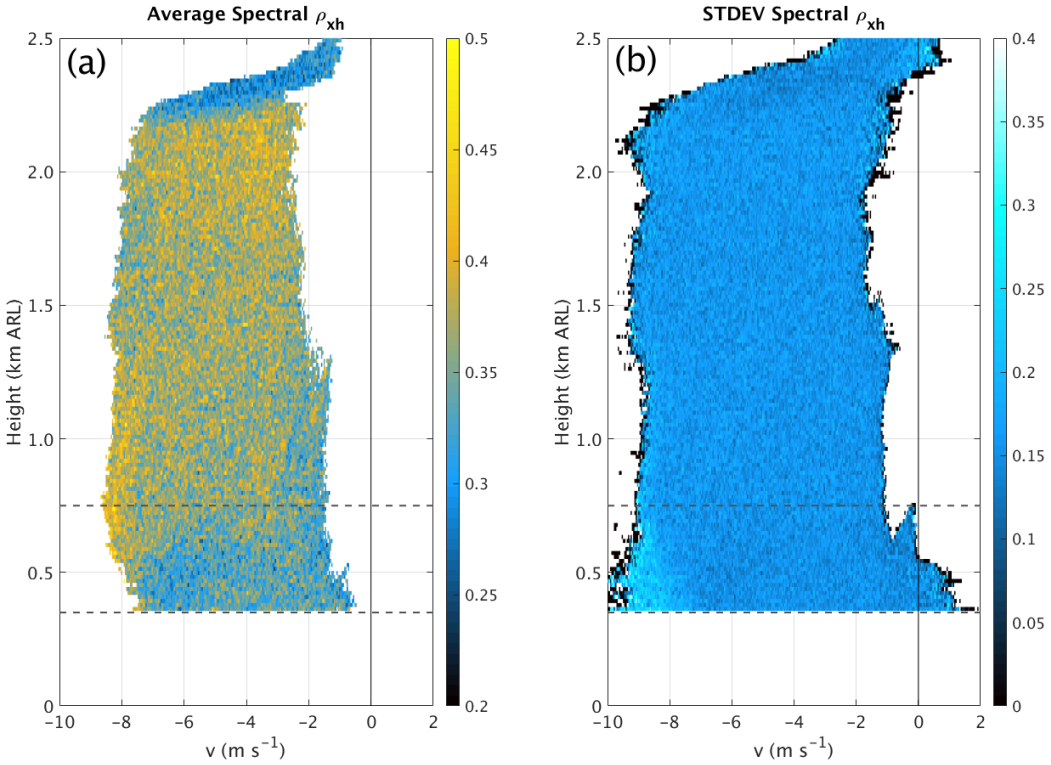

934 FIG. 14. 30-second average spectragraph of (a) spectral ρ_{xh}, and (b) its standard deviation, both shaded
935 according to the colorbars. The horizontal dashed lines represent the domain shown in Fig. 15, where refreezing
936 occurs. Data are averaged from 1821:57 to 1822:27 UTC.

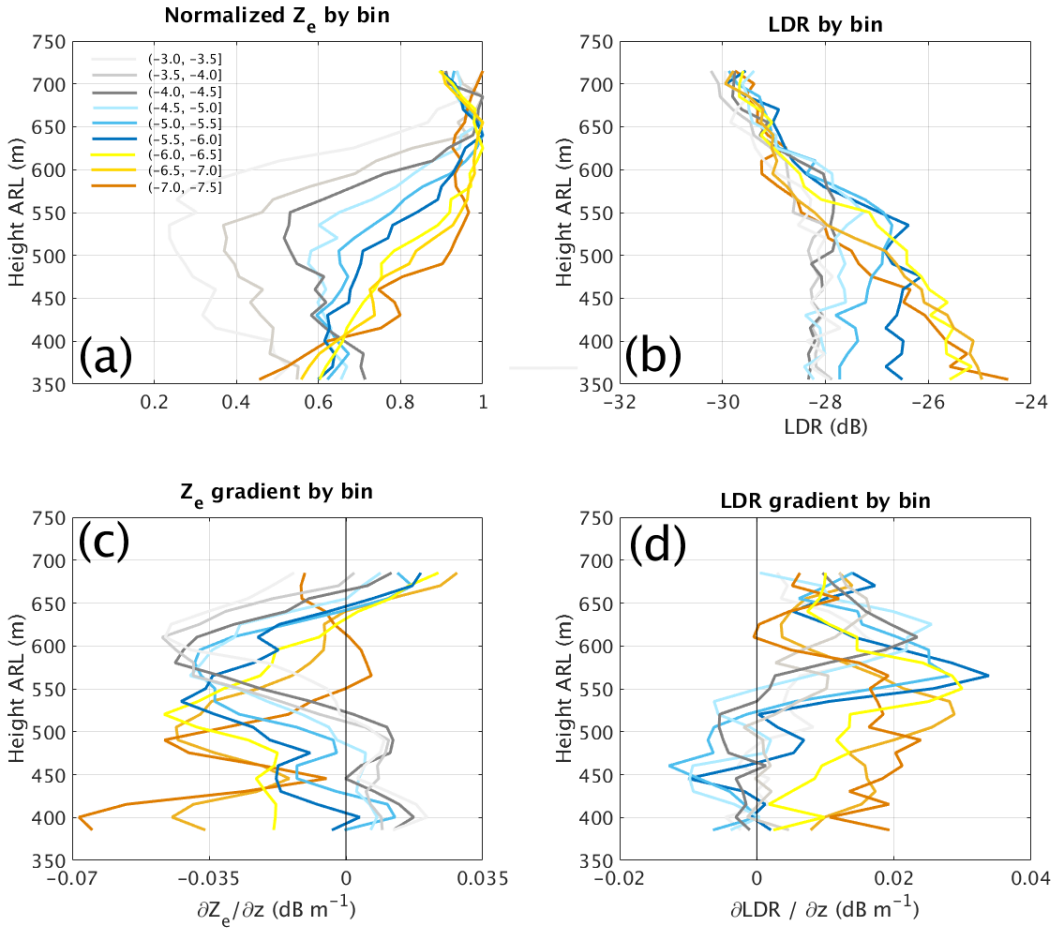

FIG. 15. (a) Vertical profiles of normalized Z_e by velocity bin (colored according to legend); (b) as in (a), but LDR by velocity bin is shown; (c) vertical gradient of Z_e by spectral velocity bin, where negative values indicate Z_e decreases towards the ground; (d) as in (c), but for LDR gradients. The data are from the 30-second averages (1821:57 to 1822:57 UTC) shown in Figs. 12-14.

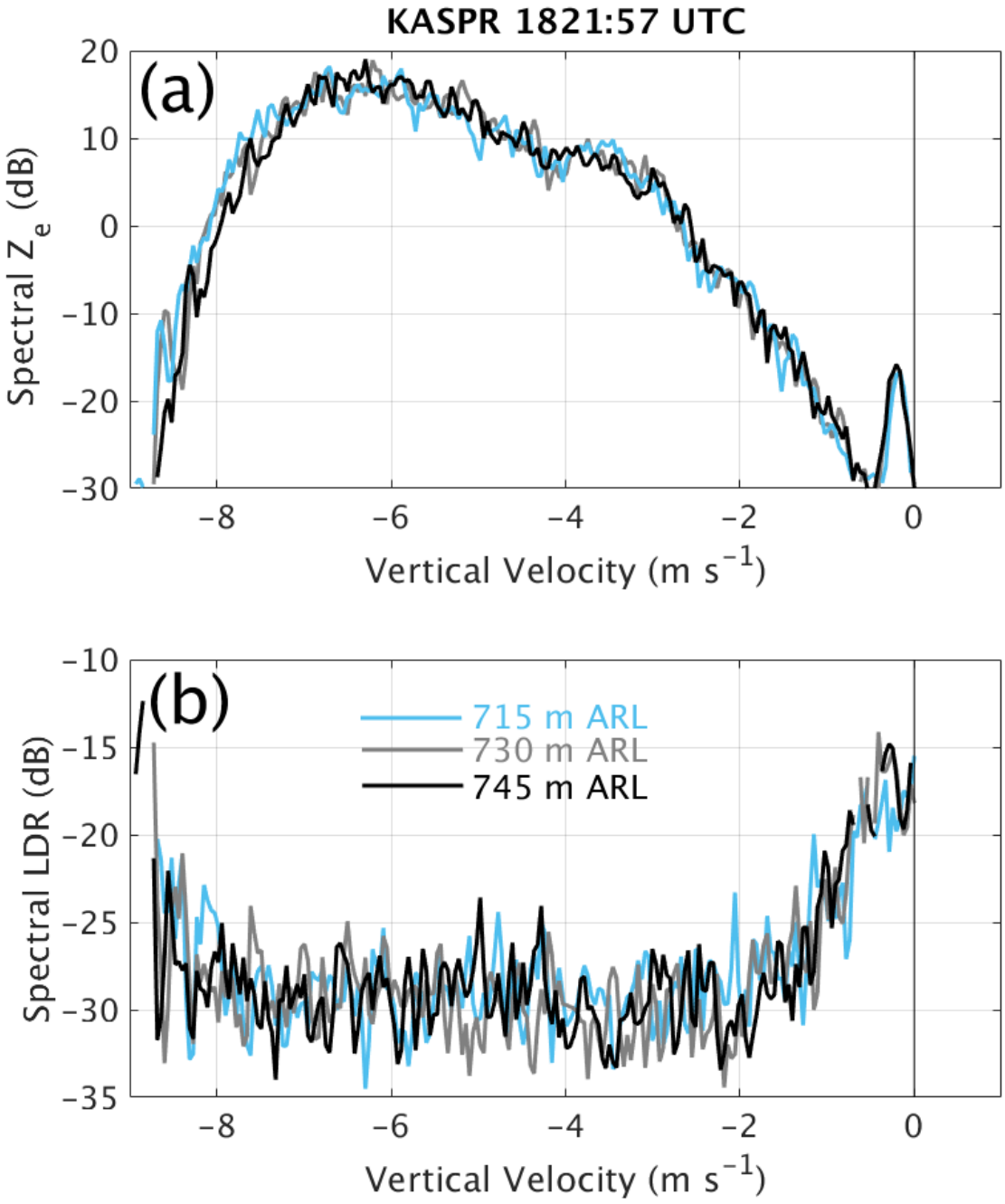

941 FIG. 16. Example 1-second Doppler spectral Z (top) and LDR (bottom) from the 1821:57 UTC vertically
942 pointing scan, at ranges 715, 730, and 745 m (colored according to legend). The co-polar power threshold used
943 here is −80 dB.

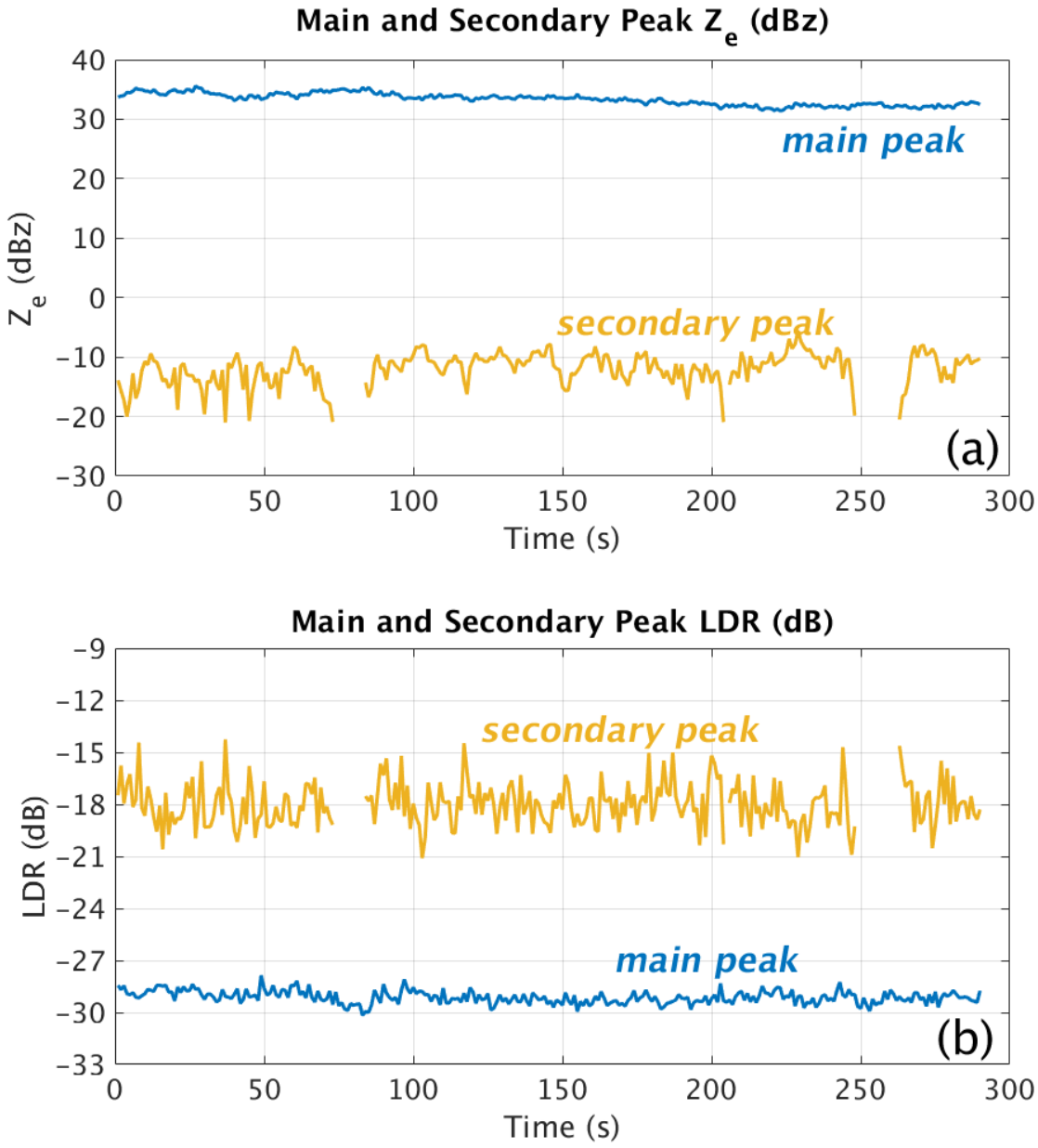

944 FIG. 17. Time series of the main (blue) and secondary (orange) peak contributions to the (a) total Z_e and (b)
945 LDR, for the five-minute period beginning at 1820 UTC. The spectra were integrated at a height of 655 m ARL.

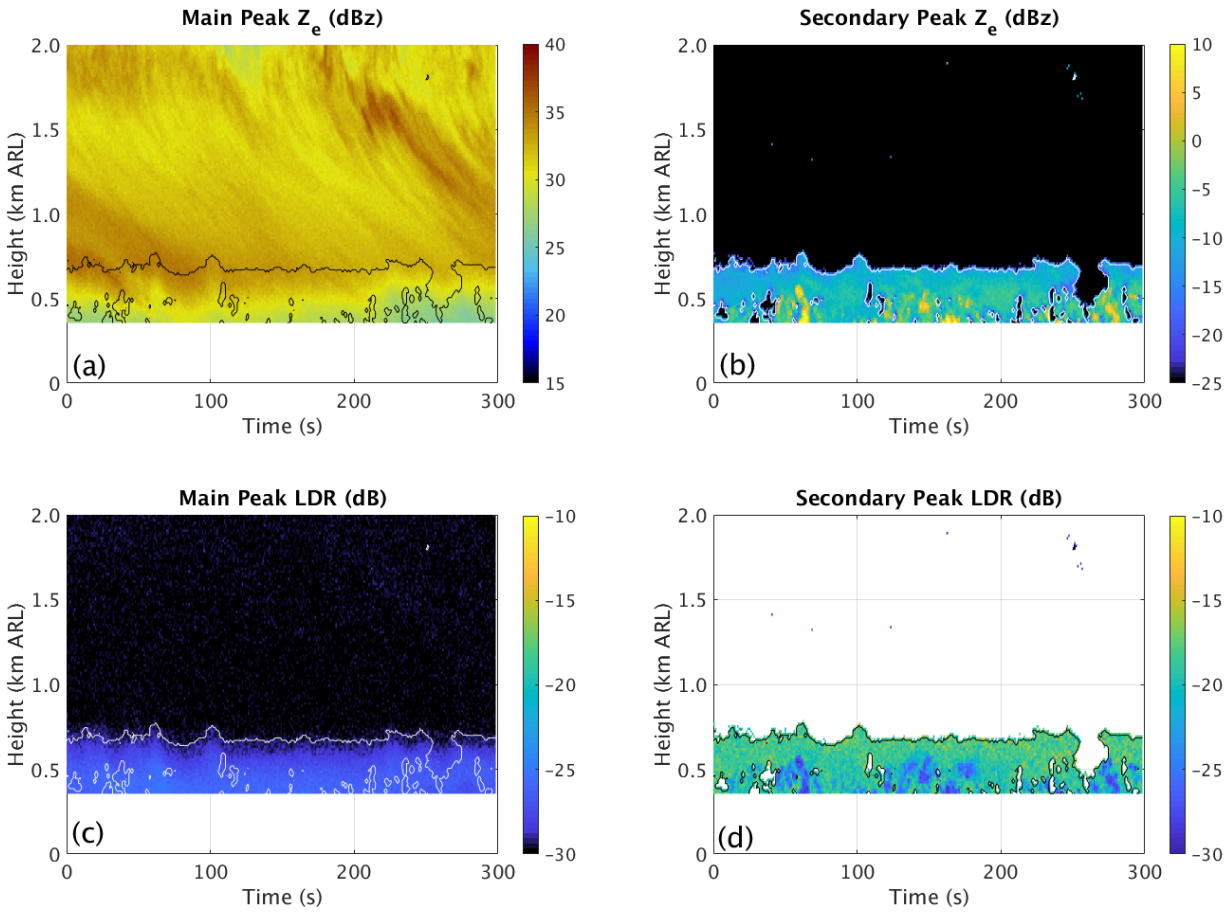

FIG. 18. Time-height depictions of the (a) main peak Z_e (dBz), (b) secondary peak Z_e (dB), (c) main peak LDR (dB), and (d) secondary peak LDR (dB). In each panel, the -19-dB contour of the secondary peak Z_e is overlaid for reference. Data shown as seconds from 1820:14 UTC.

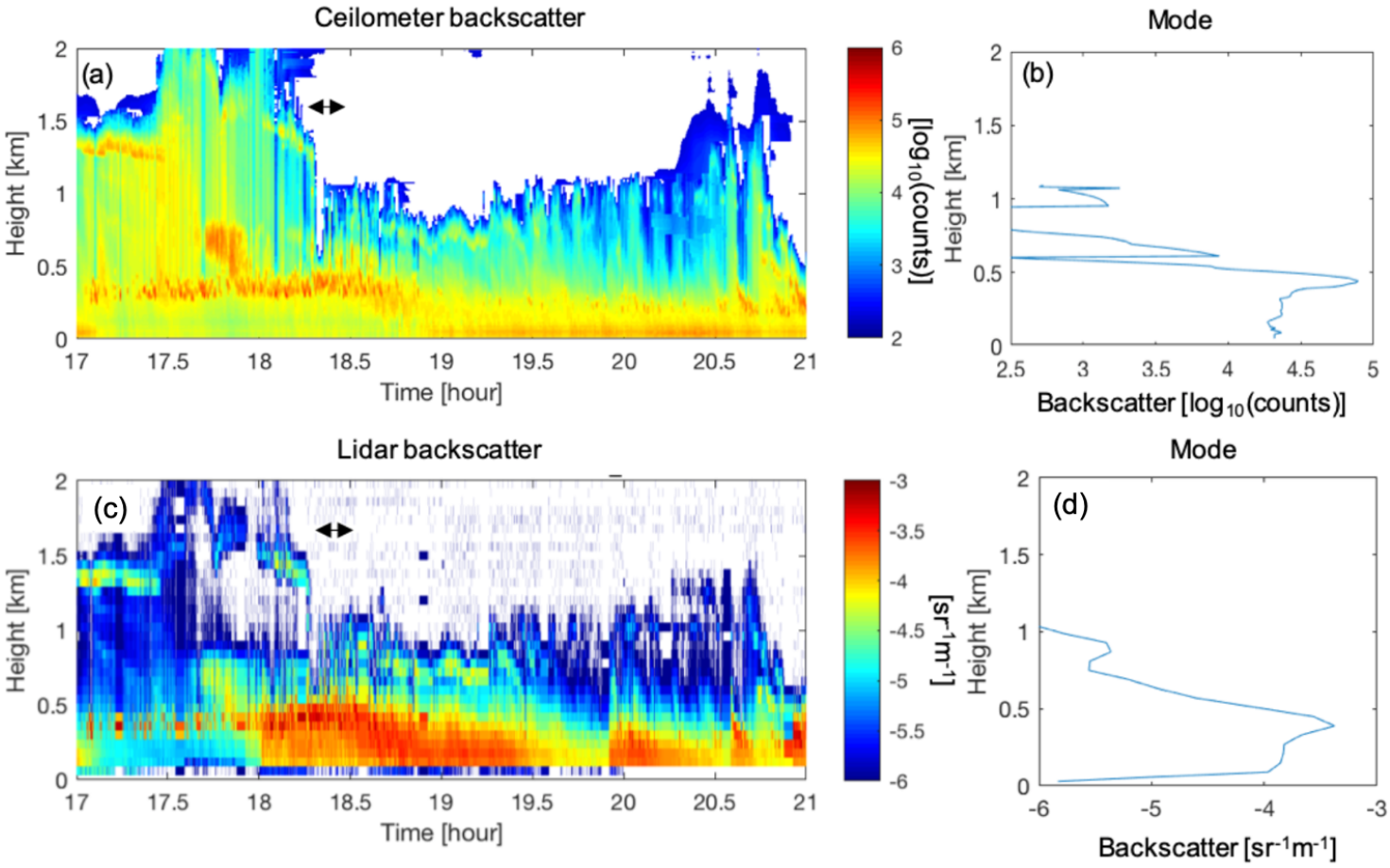

949 FIG. 19. Stony Brook University ceilometer and lidar data from the event. (a) Time-height depiction of
950 ceilometer backscatter, (b) vertical profile of the mode values of ceilometer backscatter for the 5-minute period
951 indicated by the arrows in panels (a) and (c); (c) time-height depiction of the Doppler lidar backscatter, (d)
952 vertical profile of mode values of the lidar backscatter for the 5-minute period indicated by the black arrows in
953 panels (a) and (c). The arrows indicate the time period shown in Figs. 17 and 18.

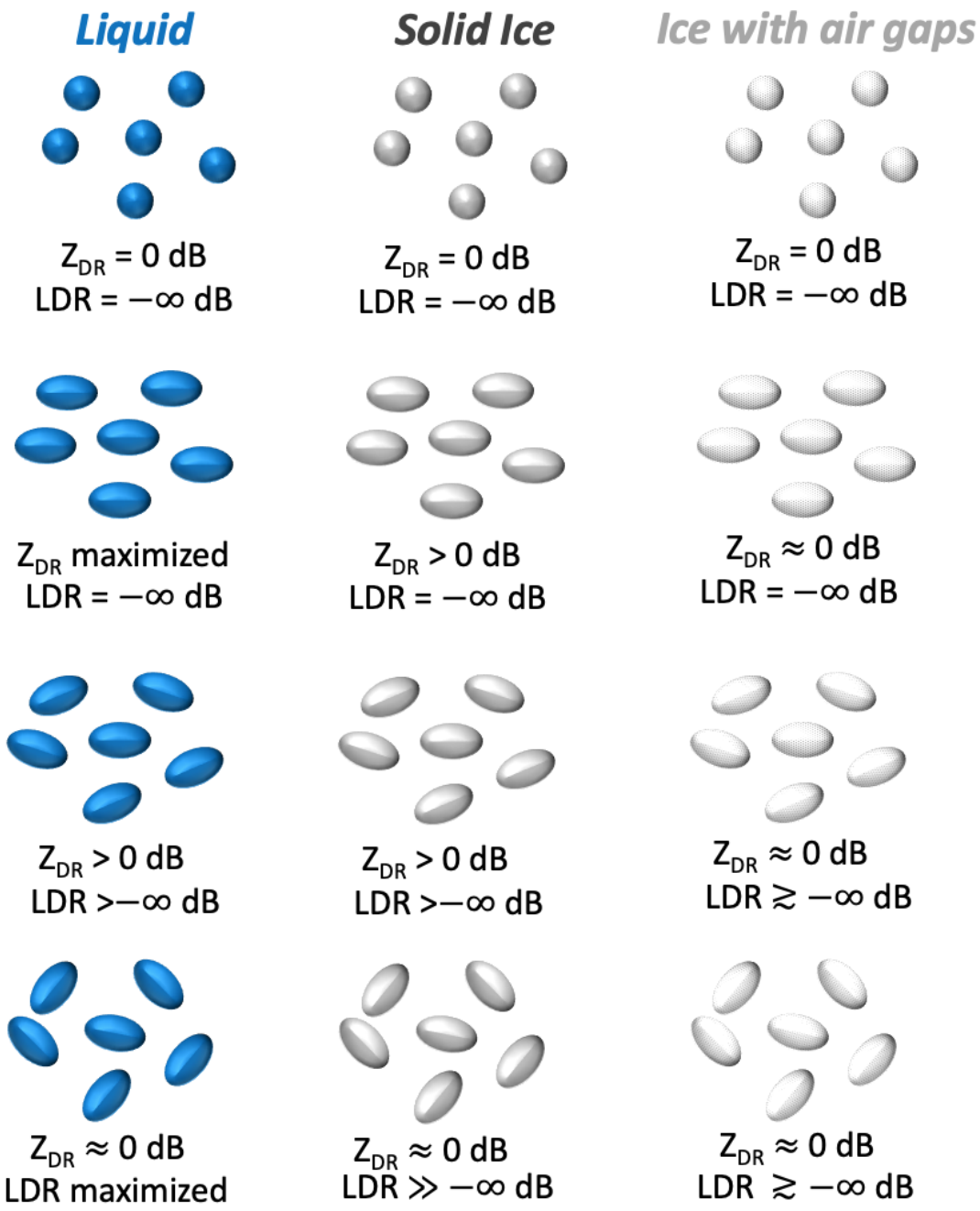

954 Fig. A1. Conceptual diagram comparing Z_{DR} and LDR for different populations of particles. In the top row,
955 the particles are all spheres. In the other rows, particles are oblate spheroids, but with increasing dispersion of
956 orientation angles as you move down each row. From left to right, the columns represent liquid particles, solid
957 ice particles, and "low-density" ice particles (i.e., particles like graupel or snow aggregates that have some air
958 pockets within the volume bounded by the particle).

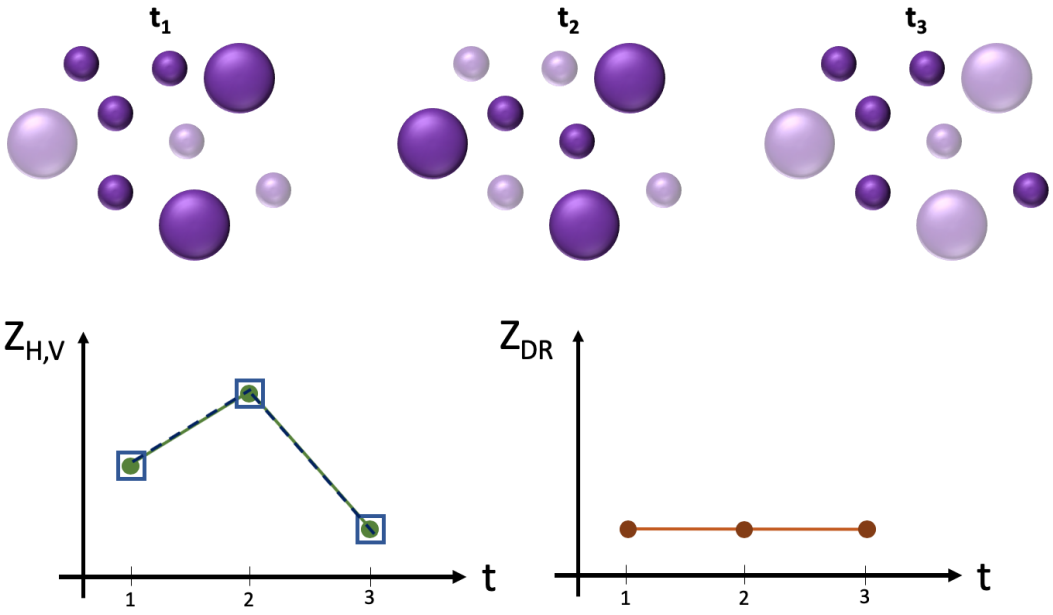

Fig. A2. Populations of spherical particles at 3 different times, with fading showing how different particles contribute more or less significantly to the overall received signal. The bottom row shows the time series of Z_H (green circle markers and line) and Z_V (blue squares and dashed line) on the left. On the right is the time series of Z_{DR} (orange circles and line).

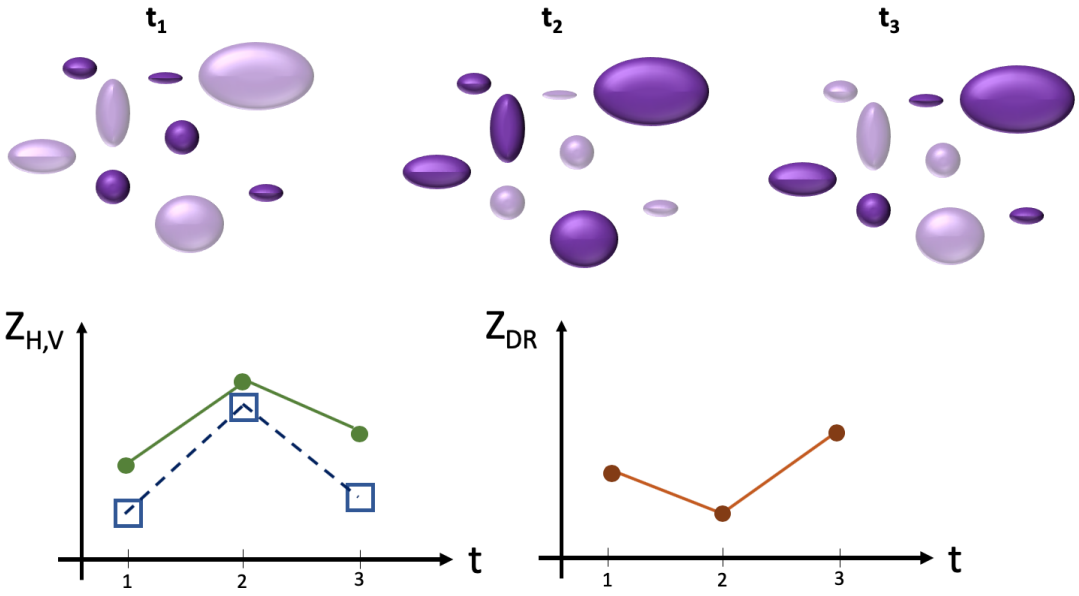

Fig. A3. As in Fig. A2, but for nonspherical particles.

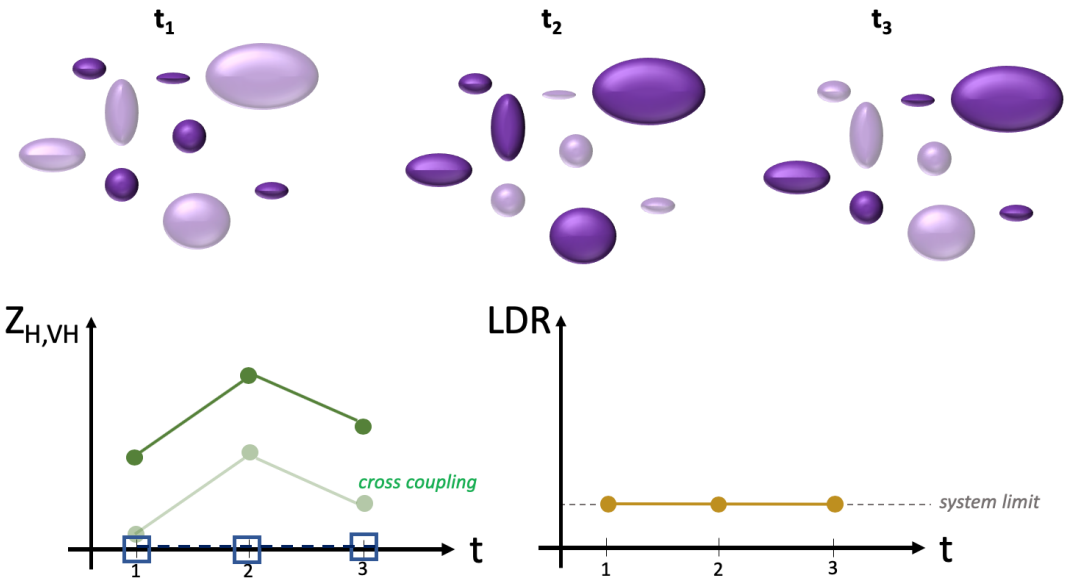

963 Fig. A4. As in Fig. A3, but the time series of Z_H and Z_{VH} are shown, as is LDR (yellow circles) on the right,

964 with the system lower limit indicated by the gray dashed line.

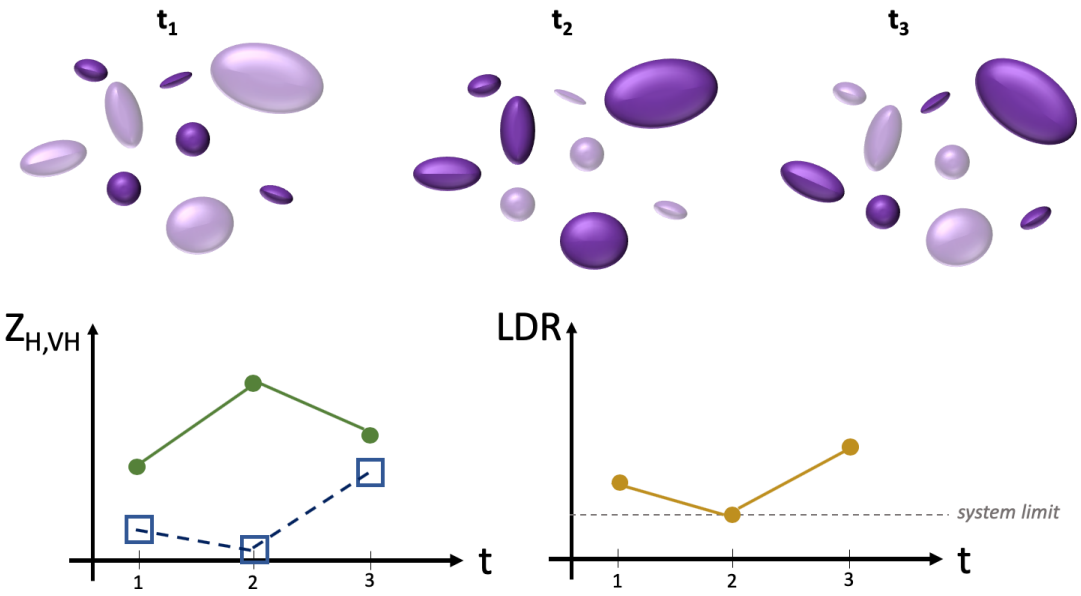

Fig. A5. As in Fig. A4, but for a dispersion of canting angles. Cross-coupling is not shown for clarity.